Creating and controlling Dirac fermions, Weyl fermions, and nodal lines in the magnetic antiperovskite Eu_3PbO

Moritz M. Hirschmann,[1,*] Alexandra S. Gibbs,[1,2,3,*] Fabio Orlandi,[2] Dmitry Khalyavin,[2] Pascal Manuel,[2] Vahideh Abdolazimi,[1] Alexander Yaresko,[1] Jürgen Nuss,[1] H. Takagi,[1,4,5] Andreas P. Schnyder,[1,†] and Andreas W. Rost[1,4,6]

[1]*Max-Planck-Institut für Festkörperforschung, Heisenbergstraße 1, D-70569 Stuttgart, Germany*
[2]*ISIS Pulsed Neutron and Muon Source, STFC, Rutherford Appleton Laboratory, Chilton, Didcot, Oxfordshire, OX11 0QX, United Kingdom*
[3]*School of Chemistry, University of St Andrews, North Haugh, St Andrews, Fife, KY16 9ST, United Kingdom*
[4]*Institute for Functional Matter and Quantum Technologies, University of Stuttgart, Pfaffenwaldring 57, D-70550 Stuttgart, Germany*
[5]*Department of Physics, The University of Tokyo, 7-3-1 Hongo, Bunkyo-ku, Tokyo 113-0033, Japan*
[6]*School of Physics and Astronomy, University of St Andrews, North Haugh, St Andrews, Fife, KY16 9SS, United Kingdom*

(Received 9 August 2022; revised 26 October 2022; accepted 28 October 2022; published 28 November 2022)

The band topology of magnetic semimetals is of interest both from the fundamental science point of view and with respect to potential spintronics and memory applications. Unfortunately, only a handful of suitable topological semimetals with magnetic order have been discovered so far. One such family that hosts these characteristics is the antiperovskites, A_3BO, a family of 3D Dirac semimetals. The A=Eu^{2+} compounds magnetically order with multiple phases as a function of the applied magnetic field. Here, by combining band structure calculations with neutron diffraction and magnetic measurements, we establish the antiperovskite Eu_3PbO as a new topological magnetic semimetal. This topological material exhibits a multitude of different topological phases with ordered Eu moments which can be easily controlled by an external magnetic field. The topological phase diagram of Eu_3PbO includes an antiferromagnetic Dirac phase, as well as ferro- and ferrimagnetic phases with both Weyl points and nodal lines. For each of these phases, we determine the bulk band dispersions, the surface states, and the topological invariants by means of *ab initio* and tight-binding calculations. Our discovery of these topological phases introduces Eu_3PbO as a new platform to study and manipulate the interplay of band topology, magnetism, and transport.

DOI: 10.1103/PhysRevMaterials.6.114202

I. INTRODUCTION

With the great success of topological band theory for insulators [1–3], recent research efforts have branched out to study the topological properties of metals and semimetals [3–7]. In contrast to ordinary semimetals, topological semimetals exhibit Fermi surfaces which are in close proximity to a band degeneracy formed by a crossing of valence and conduction bands. These band degeneracies are protected by a nontrivial topology of the electronic wave functions and give rise to a number of intriguing physical phenomena, such as ultrahigh mobility [8,9], Fermi arc or drumhead surface states [10,11], unconventional magnetoresistance [12–14], and anomalous transport properties potentially related to quantum anomalies [15–17]. Examples of topological semimetals include graphene [18], Dirac and Weyl semimetals [19–21], and nodal-line semimetals [22–25]. Besides these, there exist magnetic topological semimetals, which combine long-range magnetic order with nontrival band topology [26–48]. Unlike their nonmagnetic counterparts, these magnetic topological materials are highly tunable by external magnetic fields. In magnetic Weyl semimetals, for example, one can envision moving and manipulating Weyl points using applied fields, which in turn alters their topological transport characteristics. This property could be exploited for technological applications, e.g., for the development of next-generation spintronic devices [49].

Similar to the research on nonmagnetic topological semimetals there have been great efforts in the study of systems where magnetism coexists with band topology [26,27,27–48]. However, despite their promising potential for applications and many theoretical proposals [27–30], only a handful of promising topological magnetic Weyl semimetals has been identified so far [31–33,50]. Unfortunately, several magnetic candidate materials for topological semimetals have additional bands at the Fermi energy, which dilutes the topological transport properties [34–45]. In other cases, antiferromagnetism (AFM) occurs in centrosymmetric materials, which leads to (gapped) Dirac points instead of Weyl points [46–48].

One fundamental reason for the slow progress in finding ideal magnetic Weyl semimetals is that these are by their very nature correlated, which makes their theoretical characterization more demanding. In fact, *ab initio* calculations in general

*These authors contributed equally to this work.
†a.schnyder@fkf.mpg.de

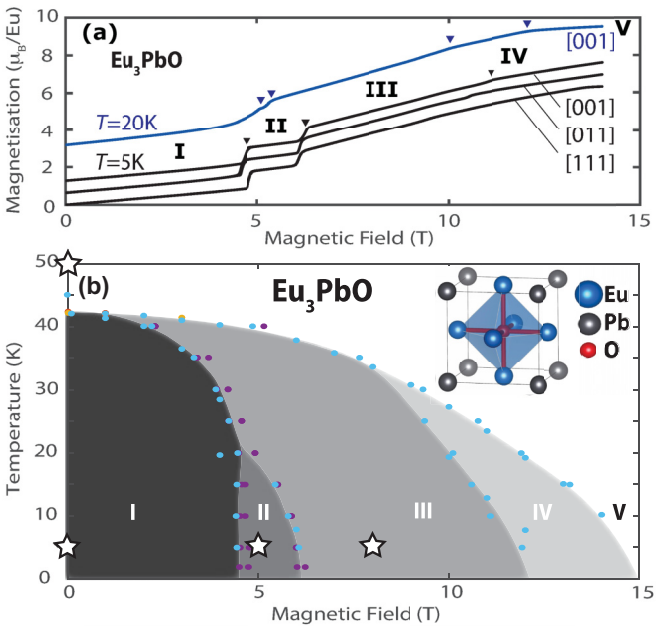

FIG. 1. Magnetic phase diagram of Eu_3PbO. (a) Magnetization of a single crystal of Eu_3PbO for several applied magnetic field directions at both 5 K and 20 K. The arrows show the location of the phase transitions with the roman numerals denoting the phases. The highest field transition to phase V is outside the field range at 5 K, but within it at 20 K. (b) The magnetic phase diagram of Eu_3PbO based on powder magnetization data, both as a function of temperature (purple) and field (blue), and specific heat measurements (orange) on powder samples. Phase I is antiferromagnetic, phases II and III ferrimagnetic, phase IV likely ferrimagnetic, and phase V fully polarized. The star-shaped markers indicate the position of our neutron scattering experimental datasets. The inset depicts the crystal structure of Eu_3PbO.

cannot predict the magnetic structure, which determines not only the magnetic symmetries but also the topological properties of the material. Hence, to characterize the topology of magnetic semimetals it is essential to combine *ab initio* band structure calculations and band topology analysis with detailed neutron diffraction measurements determining the magnetic structure. Here, we perform such a combined investigation to study the interplay of band topology with magnetism in the cubic antiperovskite Eu_3PbO [51,52]. As a function of magnetic field we observe five magnetically ordered phases: a noncollinear antiferromagnetic state at zero field, three ferrimagnetic phases at intermediate fields, and a fully polarized ferromagnetic order at large fields (Fig. 1). Using *ab initio* derived tight-binding models we determine the topological band degeneracies for each of these phases. Interestingly, we find that the antiferromagnetic state exhibits gapped Dirac cones, while the ferrimagnetic and ferromagnetic phases have Weyl points together with nodal lines. We derive the topological invariants that protect these band crossings and compute the associated surface states. Because the Weyl points in the ferri- and ferromagnetic phases act as sinks and sources of Berry flux, these phases exhibit large Berry curvatures, which enhances the anomalous Hall current.

It is remarkable that Eu_3PbO realizes such a rich variety of different magnetic topological phases, as a consequence of which the electronic structure and the band topology can be tuned and manipulated with an external field. We demonstrate that this can be achieved in two different ways: (i) by rotating the magnetization direction within a given phase and (ii) by driving Eu_3PbO across magnetic phase transitions. Through these mechanisms, it is thus possible to tune the Berry curvature of the valence and conduction bands, which in turn controls the strength of the anomalous Hall current. Hence, Eu_3PbO represents an ideal platform to study the interdependence among magnetism, band topology, and transport.

II. RESULTS

Eu_3PbO crystallizes in the cubic antiperovskite structure with space group $Pm\bar{3}m$ (No. 221). In this crystal structure (inset Fig. 1) six Eu atoms form corner-sharing octahedra, which surround the oxygen atoms. The Pb atom sits at the corner of the unit cell, surrounded by twelve Eu atoms forming a cuboctahedron. We have synthesized Eu_3PbO single crystals from stoichiometric amounts of Eu metal together with PbO [51]. Resistivity measurements confirm the expected semimetallic character and preliminary Hall conductivity measurements indicate hole doping consistent with other inverse perovskites of this series [53,54]. At zero field, Eu_3PbO orders antiferromagnetically below the Néel temperature $T_N = 42$ K (see Appendix B for susceptibility, specific heat and resistivity data) and with increasing applied field undergoes multiple phase transitions. In Fig. 1(a), we show magnetization traces for a single crystal of Eu_3PbO with the magnetic field oriented along a number of high-symmetry axes. With increasing field the material undergoes several metamagnetic transitions (indicated by arrows) and the spins become fully polarized at the saturation field of approximately 15 T. At 20 K, the transition into the fully polarized phase is observed at about 12 T, but at 5 K, it is just outside the experimentally accessible range of magnetic fields. Most importantly, the field at which the magnetic phase transitions occur is, to first order, orientation independent (although we note that there is more significant directional dependence for the phase III-IV and IV-V transitions which is outside the scope of this current work). This weak orientation dependence is also of benefit for the powder neutron diffraction measurements in an applied field, with respect to the potential for grain alignment. The fields at which neutron diffraction datasets were collected were chosen to ensure that these would correspond to single-phase measurements for the high symmetry directions shown in Fig. 1(a). Our data allow the reconstruction of the overall phase diagram, as shown in Fig. 1(b). This is based on powder measurements of specific heat (orange) as well as Quantum Design MPMS (purple) and PPMS (blue) magnetization measurements on a number of samples (see Appendix B).

The phase diagram contains, aside from the high temperature paramagnetic phase, four magnetically ordered states: one antiferromagnetic (AFM-I - labeled I) below $T_N = 42$ K and $\mu_0 H = 4.6$ T, and three ferrimagnetic within the field range 4.6–15 T (II, III, and IV), and a ferromagnetically ordered phase (FM) above approximately 15 T. All phase transitions have a reasonably strong temperature dependence as shown in the phase diagram. The metamagnetic transitions

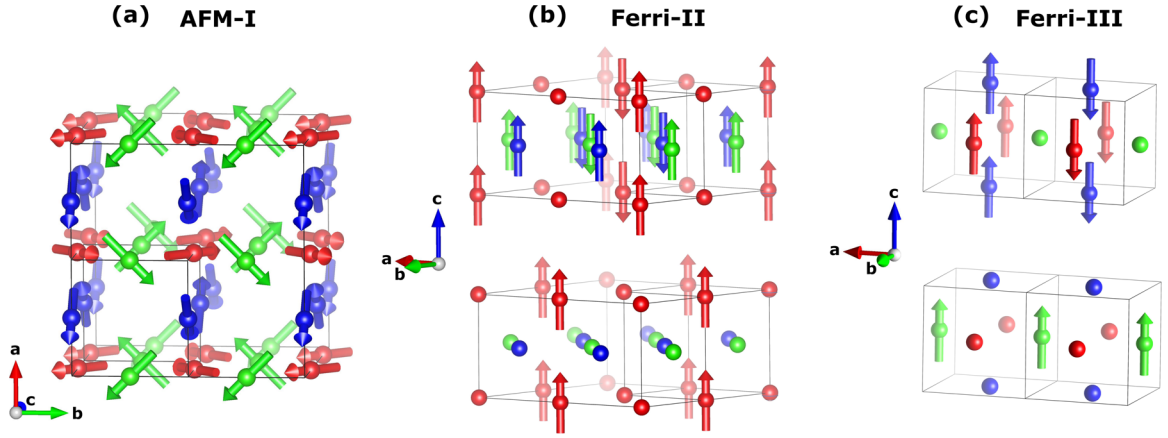

FIG. 2. (a) Schematic representation of the AFM-I magnetic structure with the magnetic space group $P_I a\bar{3}$. (b) Schematic representation of the ferrimagnetic Ferri-II structure with the $P4/mm'm'$ magnetic space group as a superposition of two components, antiferromagnetic (top) and ferromagnetic (bottom). (c) Schematic representation of the ferrimagnetic Ferri-III structure with the $Pm'm'm$ magnetic space group as a superposition of two components, antiferromagnetic (top) and ferromagnetic (bottom). In all panels, three Eu sites associated with the 3c Wyckoff position of the paramagnetic cubic $Pm\bar{3}m$ structure are shown as red, blue, and green spheres, respectively, and the paramagnetic unit cell is shown for clarity alongside the magnetic cells.

in Eu_3PbO are reproducible and consistent between multiple batches of powder and single crystal samples, confirming their robust and intrinsic nature.

A. Neutron scattering and magnetic ordering

In order to determine the magnetic structure of the magnetic phases of Eu_3PbO (excluding phase IV and the fully polarized phase V which were outwith the field range of the magnet used) we performed neutron powder diffraction measurements at the WISH beamline of ISIS, Oxfordshire UK. Above the Néel temperature T_N at zero field the refinement yields the cubic space group $Pm\bar{3}m$, with lattice parameter a = 5.0788(5) Å, in full agreement with earlier single-crystal x-ray diffraction experiments [51]. On cooling below T_N, we observe clear magnetic Bragg peaks, consistent with propagation vector $\mathbf{k} = (\frac{1}{2}, 0, 0)$. Given the extremely large number of possibilities of magnetic structures in the current case, the refinement solution underlying our analysis is the highest symmetry one consistent with the magnetic powder neutron diffraction data and the magnetic property measurements. Further details of the magnetic structure solution, along with powder diffraction patterns and fits, are given in Appendix C. Solving for the magnetic structure, the magnetic space group $P_I a\bar{3}$ (No. 205.36, type IV)[1] gives a satisfactory solution with a noncollinear antiferromagnetic spin alignment, corresponding to the action of the full arms of the propagation vector star, namely ($\frac{1}{2}$,0,0), (0,$\frac{1}{2}$,0), and (0,0,$\frac{1}{2}$) [see Figs. 2(a) and 3(b) as well as Appendix C]. This structure can be rationalized with two Eu-Eu interactions: a strong FM interaction through the oxygen and an AFM direct exchange along the octahedral edges that leads to a 120° structure.

Upon increasing the magnetic field, Eu_3PbO goes through two metamagnetic transitions at $\mu_0 H = 4.6$ T and $\mu_0 H = 6.1$ T into the two ferrimagnetic phases labeled II and III in Fig. 1 (Ferri-II and Ferri-III in Figs. 2 and 3). From our neutron measurements, we find that the Ferri-II phase has propagation vectors $\mathbf{k} = (\frac{1}{2},0,0)$, $(0,\frac{1}{2},0)$ and (0,0,0). The latter one is consistent with the development of a ferromagnetic moment. Figure 2(b) shows schematically the antiferromagnetic and ferromagnetic components of the ferrimagnetic structure. The moments are collinear and arranged in (anti)ferromagnetic and ferrimagnetic planes stacked along the b direction. Assuming that the ferromagnetic component is aligned with the field direction, a good quality fit of the magnetic intensities has been achieved in the magnetic space group $P4/mm'm'$ (No. 123.345, type III) with the magnetic structure as drawn in Figs. 2(b) and 3(c). The magnetic space group derives from the zero field one by the loss of one arm of the star of $\mathbf{k}$ corresponding to the ferromagnetic direction.

At fields above 6.1 T the Ferri-III phase is stabilized, which has a reduced symmetry with magnetic space group $Pm'm'm$ (No. 47.252, type III) by the loss of another arm of the star of $\mathbf{k}$, see Figs. 2(c) and 3(d). This magnetic structure consists of ferromagnetic planes stacked along a in a mixture of ferromagnetic and antiferromagnetic alignment to result in a net ferrimagnetic, collinear state. Above the saturation field $\mu_0 H = 15$ T, the last arm of the star is removed and Eu_3PbO becomes ferromagnetic with all spins polarized along the direction of the applied magnetic field.

We note that the identified magnetic structures map well onto the experimental magnetization data of Fig. 1. The magnetization jumps would be expected to be approximately 1.3 μ_B/Eu^{2+} at each of the 5-T and 8-T transitions, with a remaining moment ≈ 5.2 μ_B/Eu^{2+} to reach the fully polarized state. This is in good agreement with our data. We also note that there is an approximately linear background to our magnetization data which may be due to weak spin canting that we cannot determine based on powder neutron diffraction. Despite the difficulties of working with polycrystalline samples in such a high symmetry and magnetically complex material (for discussion see Appendixes C 2 and C 3) the magnetic structures determined from our neutron diffraction data constrain the magnetic structure much more effectively

[1]Here, and in what follows we use the BNS magnetic group type symbols.

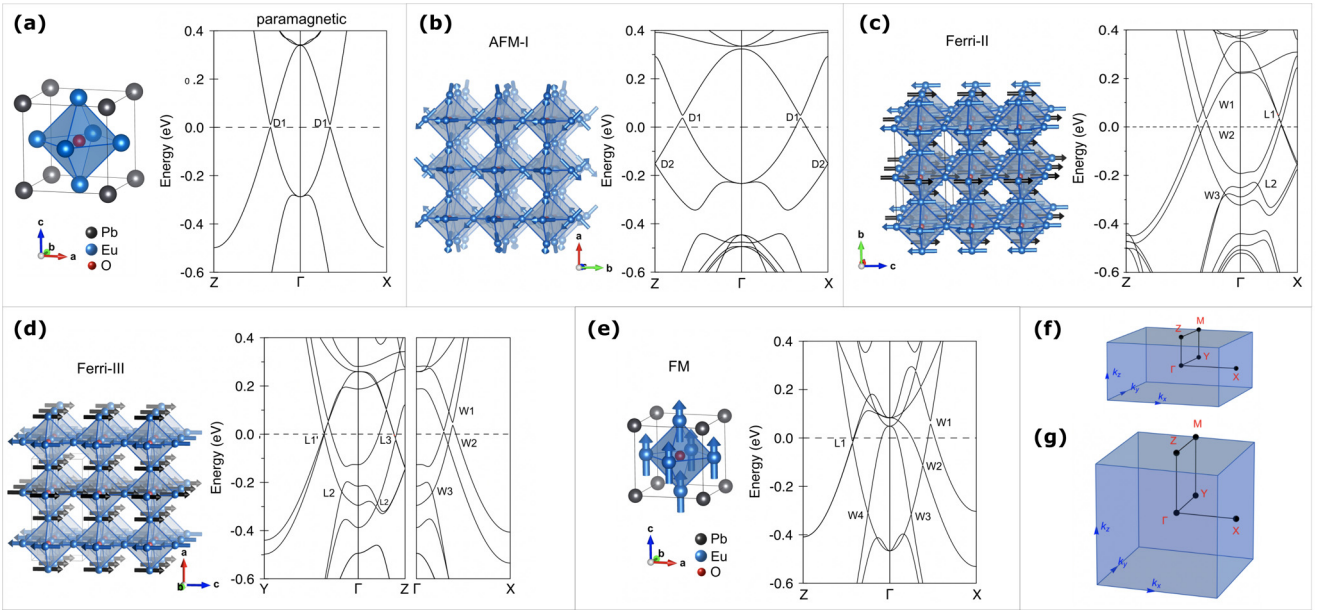

FIG. 3. Electronic band structures, magnetic orders, and Brillouin zones of Eu_3PbO. The Fermi energies are indicated by the dashed lines at 0 eV. The positions of the Dirac points, nodal lines, and Weyl points are labeled by D, L, and W, respectively, see Table I. (a) Paramagnetic phase with Brillouin zone shown in (g). (b) Antiferromagnetic phase. The paramagnetic zone is folded along Γ-X, Γ-Y, and Γ-Z, giving an eightfold increase in unit cell size. The cubic symmetry is retained and the bands are Kramers degenerate. (c) Ferri-II phase. The blue and black arrows indicate the orientations of the magnetic moments on the Eu atoms for clarity. The parent zone is backfolded halfway along Γ-X and Γ-Y. The symmetry is lowered to tetragonal. The bands are now singly degenerate except at the Weyl points and nodal lines. (d) Ferri-III phase with Brillouin zone shown in (f). The bands are back folded along Γ-Z and the symmetry is lowered to orthorhombic. The degeneracy loss is the same as for the Ferri-II phase as described above. (e) Fully polarized with field along [110]. This phase has no zone folding but loss of Kramers degeneracy and splitting of Dirac cones into Weyl points. With the field direction along [110] the symmetry is lowered to orthorhombic. Note that while in (e) the field is along [110], in all other panels the field is along [100].

than is the case for many other ferrimagnetic Weyl candidate materials where neutron diffraction studies have not been carried out.

B. Topological band structure

In the paramagnetic phase, the band structure of Eu_3PbO displays six three-dimensional Dirac cones at finite momentum along the Γ-X, Γ-Y, and Γ-Z directions that are gapped by spin-orbit coupling and an admixture of higher orbitals [54], see Fig. 3(a) and Table I. This is similar to the nonmagnetic antiperovskite Ca_3PbO [55–57], where a linear Dirac-like dispersion has recently been observed using soft x-ray ARPES measurements [58]. Indeed, just as in Ca_3PbO [57,59], the paramagnetic state of Eu_3PbO is a crystalline topological insulator characterized by two independent mirror Chern numbers [57]. This nontrivial topology arises due to a band inversion of the Eu-d and Pb-p orbitals near the Γ point and is protected by the mirror symmetries of the cubic space group $Pm\bar{3}m$. At the surface, the nontrivial band topology manifests itself by the appearance of two two-dimensional Dirac cone surface states, like in Ca_3PbO [56,57], see Fig. 4(a).

While the PM phase is very similar to the nonmagnetic antiperovskites, the magnetic phases realize a number of novel topological states. Indeed, it is expected that the different magnetic orders have significant effect on the band structure of Eu_3PbO, leading to different topological states. Let us now discuss the topological band structures of the three different magnetic phases in detail.

1. Antiferromagnetic phase

Similar to the PM phase, all bands in the AFM-I phase are twofold degenerate, even though time-reversal symmetry $\mathcal{T}$ is broken. This is because magnetic space group $P_Ia\bar{3}$ (No. 205.36) contains a symmetry element $\widetilde{\mathcal{T}}$ that combines time-reversal with a half translation along [111] (equivalent to $\{1' \mid \frac{1}{2}, \frac{1}{2}, \frac{1}{2}\}$), leading together with inversion P to Kramer's degeneracies at every $\mathbf{k}$ point. Since the AFM-I phase has an eight times larger unit cell compared to the PM phase, the electronic bands are backfolded in all three reciprocal directions, as seen by comparing Fig. 3(a) with Fig. 3(b). Backfolding leaves the six gapped Dirac points D1 of the PM phase mostly unchanged, although they are moved to a slightly higher energy (cf. Table I). Along the Γ-X, Γ-Y, and Γ-Z directions the backfolded bands hybridize and a band gap of about 100 meV opens up. At the time-reversal invariant momenta X, Y, and Z, however, hybridization is strongly suppressed by symmetry, giving rise to three (nearly) gapless Dirac points at the energy $E \simeq -0.15$ eV [D2 in Fig. 3(b)].[2] Notably, the dispersion at these Dirac crossings is linear in one direction, but quadratic in the other two.

We conclude that the AFM-I phase of Eu_3PbO contains both gapped and gapless Dirac points close to the Fermi

[2]There exists a very small, but finite hybridization between the Pb-p and Eu-d orbitals at the X, Y, and Z points, which leads to a small gap of less than 1 meV, see Appendix D.

TABLE I. Types of topological band crossings. This table lists the positions and energies of the topological band crossings in the first Brillouin zone (BZ) for the paramagnetic phase (PM), the antiferromagnetic phase (AFM), the ferrimagnetic phases (Ferri-II and Ferri-III), and the ferromagnetic phase with magnetization in [110] direction (FM [110]). The positions of the band crossings $\mathbf{k} = (k_x, k_y, k_z)$ are given in units of $2\pi/a_i$, where a_i denotes the lattice constant of the respective real space direction. All energies are given in eV relative to the Fermi energy. The type of band crossing is indicated in the fourth column, while the fifth column states the topological invariant that protects the crossings. The last column gives the multiplicity of the crossings, i.e., the number of symmetry related crossings at the same energy.

phase	position	E (eV)	type	top. inv.	#
PM	(0.18,0,0)	0.017	Dirac (D1)	mir. Chern	6
AFM-I	(0.35,0,0)	0.05	Dirac (D1)	mir. Chern	6
AFM-I	$(\pi, 0, 0)$	−0.15	Dirac (D2)	–	3
Ferri-II	(0,0,0.17)	0.07	WP (W1)	Chern	2
Ferri-II	(0, 0, 0.18)	−0.03	WP (W2)	Chern	2
Ferri-II	(0, 0, 0.07)	−0.27	WP (W3)	Chern	2
Ferri-II	k_xk_y plane	0.05	Line (L1)	Berry	1
Ferri-II	k_xk_y plane	−0.24	Line (L2)	Berry	1
Ferri-III	(0.17,0,0)	0.09	WP (W1)	Chern	2
Ferri-III	(0.16, 0, 0)	−0.04	WP (W2)	Chern	2
Ferri-III	(0.07,0,0)	−0.25	WP (W3)	Chern	2
Ferri-III	k_yk_z plane	−0.003	Line (L1')	Berry	1
Ferri-III	k_yk_z plane	−0.26	Line (L2)	Berry	1
Ferri-III	k_yk_z plane	−0.007	Line (L3)	Berry	2
FM [110]	(0.23, 0.015, 0)	0.06	WP (W1)	Chern	4
FM [110]	(0.19, −0.001, 0)	−0.12	WP (W2)	Chern	4
FM [110]	(0.12, 0, 0)	−0.32	WP (W3)	Chern	4
FM [110]	(0.003, 0.003, 0.13)	−0.31	WP (W4)	Chern	4
FM [110]	[110] plane	−0.02	Line (L1)	Berry	1

energy, within an experimentally accessible energy range. Remarkably, this is only the second known example of a Dirac state in an antiferromagnet, the other one being CuMnAs [46].

2. Ferrimagnetic phases

In the ferrimagnetic phases Ferri-II and Ferri-III, the symmetry is lowered, which results in a lifting of the Kramer's degeneracy of the bands. As a consequence, all bands are in general singly degenerate, but can form doubly degenerate Weyl points when they cross. In Table I we list the Weyl points (WP) that are close to the Fermi energy, see Fig. 3(c) and 3(d). We observe that the multiplicity of all the Weyl points is only two, i.e., due to the low symmetry there are only two Weyl points at the same energy. Such a pair of Weyl points, which are related by inversion, represents the simplest kind of Weyl band crossings. The low-energy physics near these Weyl points is described by magnetic Weyl fermions, which exhibit a number of exotic phenomena, e.g., topological (magneto)transport properties due to the chiral anomaly [5,6]. By doping Eu_3PbO with, e.g., Eu deficiencies, the Fermi level could be tuned to these pairs of Weyl points, which would allow to measure the topological transport signatures in a clear way.

The Ferri-II and Ferri-III phases exhibit in addition to the Weyl points also line crossings, where two bands intersect along a one-dimensional line in the BZ. In the Ferri-II phase these line crossings appear in the k_xk_y plane and are mapped onto themselves under inversion, resulting in multiplicity one. They are protected by the mirror symmetry $z \to -z$ and a π-Berry phase, which is expected to lead to drumhead surface states [23], whose shape depends on the chosen termination [60]. In the Ferri-III phase, the line crossings occur in the k_yk_z-plane and are protected by the mirror symmetry $x \to -x$, since here the magnetic moments point along the x direction, rather than the z direction. Contrary to the Ferri-II phase, the Ferri-III phase also exhibits a pair of nodal lines with multiplicity two (L3 in Table I). The two nodal lines of this pair are mapped onto each other by inversion symmetry.

3. Ferromagnetic phase

In the FM phase, all magnetic moments are colinearly aligned along the direction of the applied magnetic field. As a consequence, the Kramers degeneracy of the bands in the PM and AFM-I phases is lifted and the gapped Dirac points are split up into a collection of Weyl points. For concreteness, we consider here a field applied along the [110] direction, which lowers the symmetry to $Cmm'm'$ (No. 65.486) and leads to an interesting set of Weyl points and nodal lines (other field directions are discussed Appendix D). In this case, the bands near the Fermi energy form four quartets of Weyl points and one nodal line, see Fig. 3(e) and Table I. The four Weyl points of the quartets W1, W2, and W3 are located within the $k_z = 0$ plane and are symmetry related by inversion and mirror symmetry $k_x \leftrightarrow k_y$. The four Weyl points of the quartet W4 lie within the $[\bar{1}10]$ plane and are symmetry related by inversion and twofold rotation along the z axis combined with time-reversal. We remark that opposite chirality Weyl points in the quartets W1, W2, and W3 show significant separation in momentum space, which results in large arc surface states (cf. Fig. 4) and, moreover, enhances the topological transport signatures. Opposite chirality Weyl points in the quartet W4, on the other hand, are close together in $\mathbf{k}$ space, separated by only $\delta k = 0.008 \times 2\pi/a$, see Table I. Besides these Weyl points, the FM phase with [110] magnetization exhibits also a line node in the plane perpendicular to the [110] direction, which is protected by mirror symmetry.

C. Surface states

The surface states in the PM phase of Eu_3PbO, which are shown in Fig. 4(a), are similar to the nonmagnetic antiperovskites. Like in Ca_3PbO [56,57], we observe two-dimensional Dirac cone surface states, both for the lead and oxygen terminations.[3] These Dirac cone surface states appear by the bulk-boundary correspondence, as a consequence of the nonzero mirror Chern numbers that characterize the nontrivial bulk topology. Since the surface states are singly degenerate,

[3]Lead (oxygen) termination refers to surfaces that contain besides europium only lead (oxygen) atoms, cf. Ref. [57].

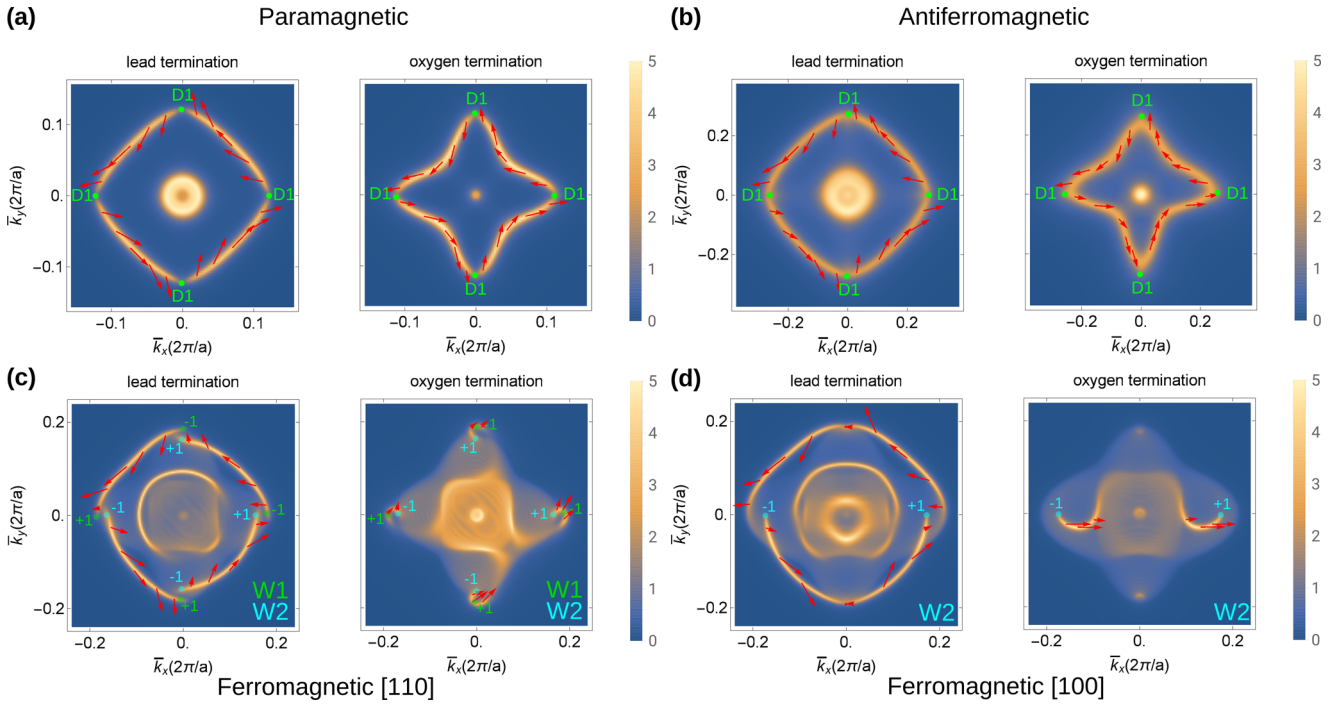

FIG. 4. Surface states of Eu_3PbO and their spin polarization. Calculated surface density of states (SDOS) and spin polarization for a [001] slab of Eu_3PbO with oxygen and lead termination. The color code represents the SDOS on a linear scale for the five outermost layers, while the in-plane spin polarization is indicated by the red arrows. (a) and (b) show the SDOS for the paramagnetic and antiferromagnetic phases at the energy of the upper Dirac points $E = 0.017$ and 0.05 eV, respectively (cf. Table I). The position of the Dirac points is marked by the label D1. (c) and (d) display the SDOS for the ferromagnetic phase with magnetization in [110] and [100] directions at the energy of the Weyl points W1 and W2, respectively. The chiralities and positions of the Weyl points W1 and W2 are indicated in all panels by the green and blue dots and numbers.

they exhibit a nontrivial spin texture, as indicated by the red arrows.

In the magnetically ordered phases of Eu_3PbO, the ordered Eu moments cause large changes not only in the bulk bands but also in the surface states. To exemplify this, we focus on the surface states of the AFM-I and FM phases.

1. Antiferromagnetic phase

In Fig. 4(b), we present the surface states of the AFM-I phase with [001] termination. We find that the surface states are qualitatively similar to the PM phase. For both the lead and the oxygen termination there appear Dirac cone surface states with a nontrivial spin polarization. Because of the backfolding of the BZ, these surface states now cover twice as much area as in Fig. 4(a). As in the PM phase, the Dirac cone surface states of the AFM-I phase are guaranteed to exist due to the bulk-boundary correspondence, which relates them to the mirror Chern number of the bulk bands.

2. Ferromagnetic phase

In the FM phase, the nontrivial topology of the Weyl points leads to the appearance of arc surface states, whose stability is guaranteed by a nonzero Chern number. The surface states on the [001] surface of the FM phase with magnetization direction [110] are shown in Fig. 4(c). For the lead termination we observe four large arc states that connect opposite chirality Weyl points of the quartets W1 and W2. Since these arc states extend over nearly half the surface BZ, they should be readily observable via quasi-particle interference in Fourier-transform scanning tunneling spectroscopy [61]. For the oxygen termination, on the other hand, the arc states are much shorter, connecting opposite chirality Weyl points that are located next to each other. Regarding the spin polarization of the arc states, we find that for the lead termination the polarization is similar to the one of the Dirac states in the PM and AFM-I phases. For the oxygen termination, however, the spin polarization points predominantly along the direction of the Eu moments. This is because for the oxygen termination, there are no Pb atoms and twice as many Eu atoms on the surface compared to the lead termination. Hence, the surface states on the oxygen termination have mostly Eu-d orbital character, while for the lead termination they have Pb-p character. For this reason, the surface states on the oxygen termination are polarized more strongly by the Eu moments than on the lead termination.

So far we have assumed that the Eu moments point along the [110] direction. However, in a single crystal it is possible to adjust the magnetization direction by aligning the spins using the external field. This allows us to tune the electronic structure and band topology of Eu_3PbO. To demonstrate this, let us consider the FM phase with the Eu moments oriented along the [100] axis. With this magnetization direction, the Weyl points W2 and W3 are slightly shifted in energy, while the W1 points are entirely absent (Appendix D). Correspondingly, the arc surface states show different

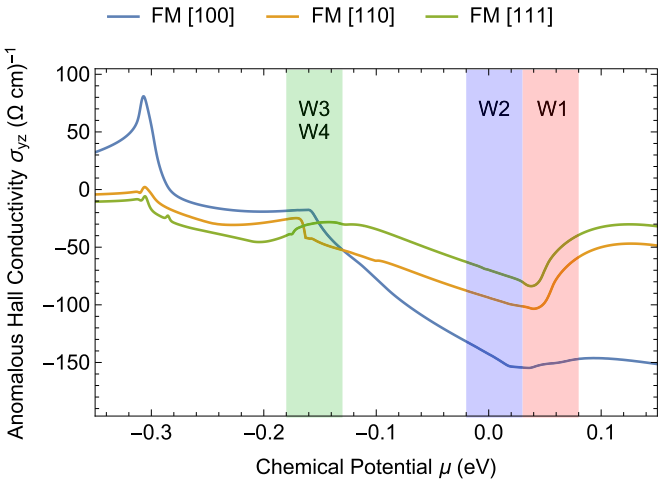

FIG. 5. Intrinsic anomalous Hall conductivity. Calculation of the intrinsic anomalous Hall conductivity σ_{yz} in the ferromagnetic phase as a function of chemical potential μ, for different magnetization directions at a temperature of 10 K. Shaded regions highlight broad features in σ_{yz} that are attributed to different Weyl points.

connectivities, see Fig. 4(d). That is, on the [100] surface, there appears a single arc state that connects the two Weyl points W2, both for the lead and oxygen terminations. (For the lead termination there is a secondary surface state feature, which however has no topological origin.)

D. Anomalous Hall conductivity

The nontrivial band topology of Eu_3PbO manifests itself not only in the surface states but also in anomalous transport characteristics, such as the anomalous Hall effect, the anomalous Nernst effect [62], or the circular photogalvanic effect [63]. For instance, the intrinsic anomalous Hall conductivity (AHC) σ_{ij} is directly proportional to the momentum integrated Berry curvature. The AHC shows local extrema when the chemical potential is tuned to the Weyl point energies. Moreover, the dependence of the band topology on the magnetic phase and the magnetization direction is expected to reflect itself in the AHC. While current single crystal sample dimensions do not allow for unambiguous experimental determination of the AHC we nevertheless include here a short discussion of the expected signatures.

To exemplify this, we calculate the intrinsic AHC σ_{yz} for the FM phase with different magnetization directions as a function of chemical potential μ (Fig. 5). We observe that the overall magnitude as well as the position of the local extrema changes with magnetization direction. For small hole doping at $\mu \simeq -0.05$ eV, the AHC in the FM phase with [110] and [111] magnetization is about 50 $(\Omega\text{cm})^{-1}$, while in the FM phases with [100] magnetization the AHC is three times larger. This is quite sizable and comparable to the values of MnSi [64] and Mn_3Sn [35]. The broad features in σ_{yz} at $\mu \simeq +0.05$ and $\mu \simeq -0.15$ originate from the Weyl points W1/W2 and W3/W4, respectively (Appendix E). Interestingly, at $\mu \simeq +0.05$ W1 gives a positive contribution, while W2 contributes negatively, because these two sets of Weyl points have opposite chiralities. Due to this cancellation, the AHC for the [110] and [111] magnetizations is about twice smaller than for the [100] magnetization, for which the Weyl points W1 do not exist.

III. SUMMARY AND DISCUSSION

Combining magnetization measurements with neutron diffraction and electronic structure calculations, we have studied the interplay between band topology and magnetism in the antiperovskite Eu_3PbO. We have discovered four different magnetic phases and identified their magnetic structures as a function of magnetic field. For each of these phases, we have determined the band topology, thereby uncovering a rich variety of Weyl points, Dirac points, and nodal lines close to the Fermi energy. Among the exemplary properties of Eu_3PbO are, for example, (i) the large Weyl point distance of, e.g., 46% of the Brillouin zone in the ferromagnetic phase, (ii) the large tunability by magnetic field through the rich phase diagram, and (iii) the fact that additional band crossings do not mask the desired physics in, e.g., the anomalous Hall effect.

By the bulk-boundary correspondence, this nontrivial topology of the bulk bands leads to various types of surface states, e.g., Dirac cone, Fermi arc, and drumhead surface states, within an easily accessible magnetic phase diagram in a single compound. Moreover, from a nontrivial bulk topology, one may expect unusual transport phenomena, such as anomalous Hall currents [65]. We have calculated the anomalous Hall conductivity of Eu_3PbO in the ferromagnetic phase and shown that it displays clear fingerprints of the Weyl points. At the metamagnetic transitions the anomalous Hall current exhibits sharp singularities, due to the rearrangement of the magnetic spin texture. Thus the different (noncollinear) magnetic orders in Eu_3PbO offer the unique opportunity to explore the sensitivity of the anomalous Hall current on the details of the magnetic structure.

The four magnetic phases of Eu_3PbO with their different band topologies can be easily accessed and manipulated with an external field. This allows to tune the electronic structure and drive it through topological phase transitions. For example, the Dirac points of the antiferromagnetic phase can be split into Weyl points by crossing the phase boundary into the ferrimagnetic phase. Furthermore, the Weyl points and line nodes of the ferri- and ferromagnetic phases can be pair-annihilated or moved in energy and momentum by adjusting the magnetization direction. This, in turn, modifies the Berry curvature of the bands, and hence the anomalous Hall conductivity. In addition nodal lines may gap along certain directions by broken mirror symmetries (i.e., change in magnetic field direction) and can substantially contribute to the anomalous Hall conductivity as discussed by, e.g., K. Kim *et al.* [66]. Exploration of the detailed field-angle phase diagram are of experimental and theoretical interest both for the magnetism stabilized in Eu_3PbO in itself as well as the impact on the topological properties of the material. Overall the rich phase diagram with interdependent magnetism, topology of the electronic bands, and anomalous transport properties makes Eu_3PbO a potential candidate for new device applications that rely on magnetic-field induced switching of topological currents, especially in light of the advances in the thin film growth of the related compound Sr_3PbO [67].

In closing, we discuss several possible directions for future experimental and theoretical studies. First, the bulk and surface Dirac cones of the paramagnetic and antiferromagnetic phases could be measured by ARPES, since these phases have no net magnetic moment. The bulk Weyl cones and surface arcs of the ferri- and ferromagnetic phases, on the other hand, could be observable in Fourier-transform scanning tunneling spectroscopy. Second, Hall resistivity and magnetoconductance measurements on single crystals are of high interest, as these would reveal transport signatures of the Weyl points and nodal lines. Third, Nernst effect and magnetothermal transport measurements could provide a direct measure of the Berry curvature [62]. Furthermore, they could reveal possible violations of the Wiedemann-Franz law, due to the chiral anomaly of the Weyl points [68]. We note that single crystals of Eu_3PbO are naturally hole doped, such that the Dirac and Weyl points D2 and W2 should be readily accessible in transport and ARPES measurements. On the theoretical side, it would be interesting to investigate the RKKY interactions among the Eu moments and to study effects of magnetic and Coulomb interactions and disorder on the band topology. We hope that our work will inspire future research along these lines.

ACKNOWLEDGMENTS

We gratefully acknowledge useful discussions with A. Bangura, A. Leonhardt, H. Nakamura, and T. Kariyado. We thank the Science and Technology Facilities Council for beamtime under RB1700035. We wish to thank R. Kremer and E. Brücher for physical property measurements. A. W. R. and A. S. G. were supported by the Engineering and Physical Sciences Research Council (Grants No. EP/P024564/1 and No. EP/T011130/1, respectively). This work has been supported in part by the Alexander von Humboldt Foundation.

APPENDIX A: OVERVIEW OF METHODS

1. Electronic structure calculations and tight-binding model

The electronic structure of Eu_3PbO was computed by a relativistic linear muffin-tin orbital calculation [69,70] using the in-house PY LMTO computer code as described in Ref. [70]. The code is available on demand. As an input for the DFT calculation we used the experimental crystal structure of Ref. [51]. The DFT calculations show that the bands near the Fermi energy originate mostly from Pb-p and Eu-d orbitals. Guided by these observations, we use the Pb-p and Eu-d orbitals as a basis set to derive a nine-band tight-binding model. With this tight-binding model we have computed the surface states, the Berry curvature, and the topological invariants. The details of the tight-binding model are presented in Appendix D.

2. Topological invariants, surface states, and anomalous Hall conductivity

The stability of the Dirac, Weyl, and nodal-line band crossings is guaranteed by nonzero topological invariants. We have numerically computed these topological invariants using the tight-binding model, see Appendix E 1. By the bulk-boundary correspondence a nonzero value of the topological invariant leads to protected surface states. Using the tight-binding model we have computed the density of states and spin polarization of these surface states, which are presented in Fig. 4. The anomalous Hall conductivity is obtained from the momentum integral of the Berry curvature, see Appendix E 2.

3. Crystal growth and sample characterization

Crystals of Eu_3PbO were grown in a sealed Ta ampoule as reported previously in Ref. [51]. Since Eu_3PbO is extremely air sensitive, all experiments were prepared and sealed under Ar atmosphere. Single crystals for magnetization measurements were covered by a thin layer of Apiezon N grease to protect it from air during transfer. All magnetization measurements were performed both in a Quantum Design SQUID as well as with the VSM option in a Quantum Design PPMS system.

4. Neutron scattering measurements

Neutron scattering measurements were performed at the WISH beamline of ISIS, Harwell, Oxford. Polycrystalline Eu_3PbO was used for all of the neutron diffraction measurements. Isotope enrichment was not possible due to the necessity of using Eu as a reagent, rather than Eu_2O_3. In zero field, a loose powder was contained in a cylindrical 1 mm diameter suprasil capillary (sealed under 200 mbar He to provide exchange gas and prevent sample decomposition) which was then held in a vanadium can for the measurement. A pelletized sample was used for the applied field measurements to prevent grain alignment in applied field, this was contained in a flattened suprasil ampoule to prevent movement and again was sealed under He atmosphere. Data were collected at 50 K and 1.5 K for the loose powder sample and 50 K at 0 T, 1.5 K at 0 T followed by 1.5 K at 5 T and 1.5 K at 8 T without intermediate warming. For the details on the magnetic structure determination see Appendix C.

APPENDIX B: SPECIFIC HEAT AND SUSCEPTIBILITY MEASUREMENTS

Here we briefly present further physical property measurements underlying the phase diagram presented in the main text. In Fig. 6, we present magnetic susceptibility (top), specific heat (middle), and resistivity (bottom) data of Eu_3PbO.

The magnetic susceptibility was measured on a powder sample in a field of 100 Oe and shows a clear transition into the antiferromagnetic phase at ca. 40 K. Above T_N a clear Curie-Weiss behavior is observed corresponding to a magnetic moment of 7.8 μ_B consistent with the expected moment for Eu^{2+}.

Specific heat was measured in zero field on a pressed pellet in a Quantum Design PPMS system. The transition into the antiferromagnetic state is clearly observable at T_N.

Finally we present resistivity measurements again on a pressed pellet. While low temperature transport is dominated by grain boundaries the semi-metallic behavior at higher temperatures as well as the transition into the antiferromagnetic state is readily discernible. Especially the latter indicates a

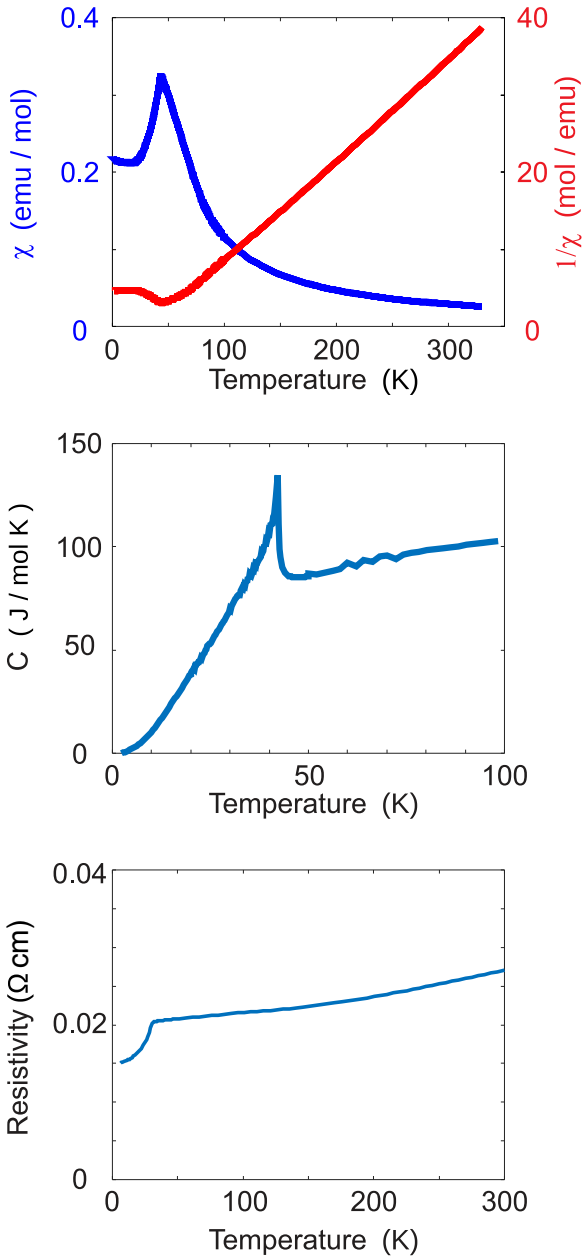

FIG. 6. Magnetic susceptibility (top), specific heat (middle), and resistivity (bottom) of Eu_3PbO. For more details see text.

strong coupling of the magnetic order with electronic transport.

APPENDIX C: DETERMINATION OF THE MAGNETIC STRUCTURES

Polycrystalline Eu_3PbO was used for all of the neutron diffraction measurements. In zero field a loose powder was contained in a cylindrical 1 mm diameter suprasil capillary (sealed under 200 mbar He to provide exchange gas and prevent sample decomposition) which was then held in a vanadium can for the measurement. A pelletized sample was used for the applied field measurements to prevent grain alignment. This was contained in a flattened suprasil ampoule to prevent movement under applied field and again was sealed under He atmosphere. Data were collected at 50 K and 1.5 K for the loose powder sample and 50 K at 0 T, 1.5 K at 0 T followed by 1.5 K at 5 T and 1.5 K at 8 T without intermediate warming.

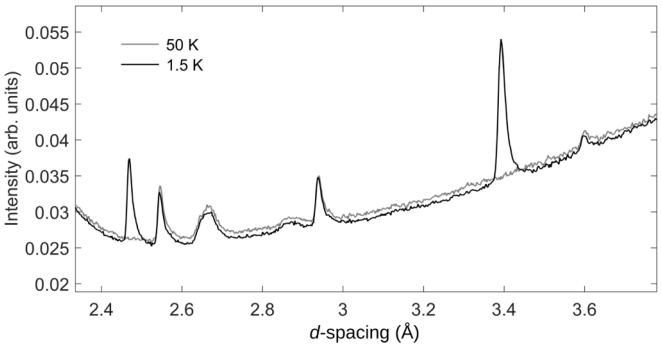

FIG. 7. The paramagnetic (50 K) and antiferromagnetic (1.5 K) phase data from banks 3 and 8 of WISH. The substantial background is from the quartz ampoule used to contain the sample.

1. Crystal structure of Eu_3PbO

At 50 K in zero field, a good structural refinement could be obtained in $Pm\bar{3}m$, in good agreement with previous powder and single crystal x-ray diffraction studies, with a = 5.0788(5)Å. The setting with Eu on Wyckoff site 3*c* (0,1/2,1/2), Pb on site 1*a* (0,0,0) and O on site 1*b* (1/2,1/2,1/2) was used throughout.

2. Zero field magnetic structure

In the 1.5 K data, magnetic Bragg peaks were observed (see Fig. 7), consistent with a propagation vector of $\mathbf{k} = (1/2, 0, 0)$. The magnetic structure solution began with the assumption (supported by magnetometry) that a finite ordered moment must be present on all Eu sites. The maximal magnetic subgroups of $Pm\bar{3}m1'$ for propagation vector $\mathbf{k} = (1/2, 0, 0)$, considering a single arm only, and a magnetic ion on the 3*d* site were investigated using the MAXMAGN tool of the Bilbao Crystallographic Server [71], but none satisfied the above condition.

Following this, the tool k_Subgroupsmag [72] was used to determine the subgroups of $Pm\bar{3}m1'$ which fulfill this condition. These subgroups were investigated in order of decreasing symmetry by examination of systematic absences followed by Rietveld refinement using FULLPROF and JANA2006 of potential candidates [73,74].

Systematic absences violations excluded $P_c\bar{4}c2$, P_c4cc, and P_ccc2. Rietveld refinements were performed using magnetic-only datasets created by subtracting the 50 K paramagnetic

TABLE II. The results of the Rietveld refinement of the 1.5K 0T Eu_3PbO data in magnetic space group A_ama2, in the standard setting where $a = \sqrt{2}a_p$, $b = \sqrt{2}a_p$, $c = 2a_p$, and a_p is the parent lattice constant $a_p = 5.0763(13)$ Å.

Site	*x*	*y*	*z*	m_x (μ_B/Eu^{2+})	m_y (μ_B/Eu^{2+})	m_z (μ_B/Eu^{2+})
Eu1	0.75	0.25	0.25	7.49(8) ±0.08	0	0
Eu2	0	0	0.0	0	0	2.57 ±0.14

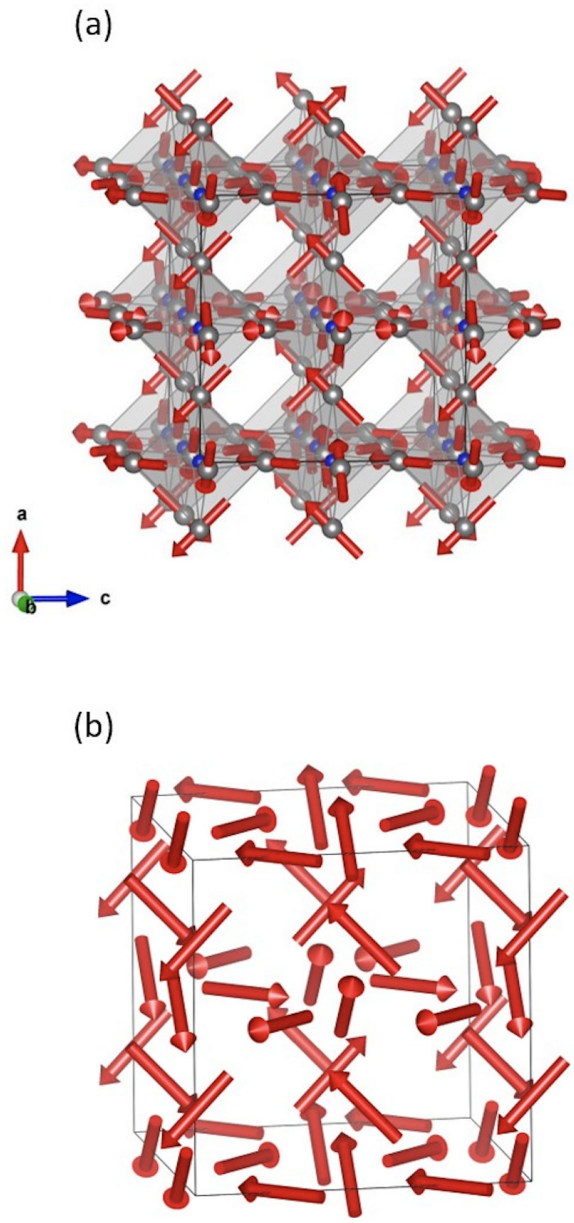

FIG. 8. The zero-field magnetic structure of Eu_3PbO (top) and spin-only representation (bottom).

data from the 1.5 K data. The scale and absorption factors were fixed by a refinement of the nuclear phase with the 50 K dataset. A_ama2 (BNS 40.208) with transformation matrix (2c, -$a+b$, $a+b$), origin shift (0,0,1/2) was the only direct subgroup of $Pm\bar{3}m1'$ in the tree under consideration found to give a satisfactory refinement and therefore no further symmetry lowering was investigated. The results of the refinement can be found in Table II. The moment obtained for Eu1 is slightly in excess of the expected ordered moment. In addition, the moments on the two Eu sites are perpendicular which is not easily rationalized. Since the different moment sizes as well as orientation are not reconcilable with physical property measurements we can exclude this single-k solution.

However, the data are consistent with a multi-k structure with the use of the full arm of the star: $\mathbf{k}_1 = (1/2, 0, 0)$, $\mathbf{k}_2 = (0, 1/2, 0)$, and $\mathbf{k}_3 = (0, 0, 1/2)$. There are a large number of possible structures consistent with these vectors, with differing moment directions relative to the lattice. However, in the cubic metric this cannot be determined from powder data. Therefore the highest symmetry option consistent with the data, $P_Ia\bar{3}$ with a single Eu site, was investigated and found to give a satisfactory fit, with a reasonable ordered moment. Other cubic magnetic space groups consistent with the propagation vectors can be ruled out by systematic absence considerations.

TABLE III. The results of the Rietveld refinement of the 1.5K 0T Eu_3PbO data in magnetic space group $P_Ia\bar{3}$, in the standard setting where a $= 2a_p$, b $= 2a_p$, c $= 2a_p$, and a_p is the parent lattice constant a = 10.15638(10) Å.

Site	x	y	z	m_x (μ_B/Eu^{2+})	m_y (μ_B/Eu^{2+})	m_z (μ_B/Eu^{2+})
Eu1	0	0.5	0.25	0	-4.769 ± 0.011	4.769 ± 0.011

This structure can be rationalized with two Eu-Eu interactions: a strong FM interaction through the oxygen and an AFM direct exchange along the octahedral edges that leads to a 120° structure, as shown in Fig. 8. The refinement results are tabulated in Table III, and fitted profiles are shown in Fig. 9. Since this model gives a reasonable ordered moment for a single Eu site, and with the current data we cannot distinguish between single- and multi-k order, we have taken the multi-k $P_Ia\bar{3}$ model as the most appropriate for the zero-field state, since it can be easily rationalized using the known interactions of Eu^{2+}.

3. Applied field magnetic structures

The $P_Ia\bar{3}$ model allows for a simple evolution of the structure with applied magnetic field, with the magnetic structure losing one arm of the star of **k** at each magnetic transition (we consider field applied along the c axis). The addition of propagation vector (0,0,0) captures the ferromagnetic moment. For the first transition at 5 T the propagation vector $(0,0,\frac{1}{2})$ is lost (see Fig. 10) and a model in $P4/mm'm'$ with five Eu sites, constrained to have equal moment, gives an excellent fit and reasonable ordered moment (see results in Table IV and

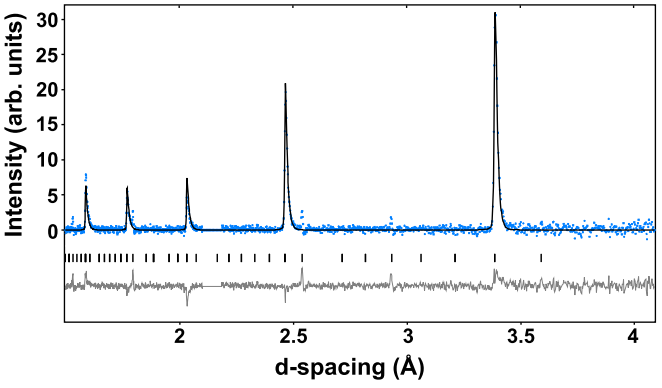

FIG. 9. A portion of the Rietveld refinement for the $P_Ia\bar{3}$ structure (90° banks 3 and 8 WISH, magnetic only subtracted pattern) with the data in blue, calculated pattern in black, difference in gray, magnetic reflections indicated by black tickmarks.

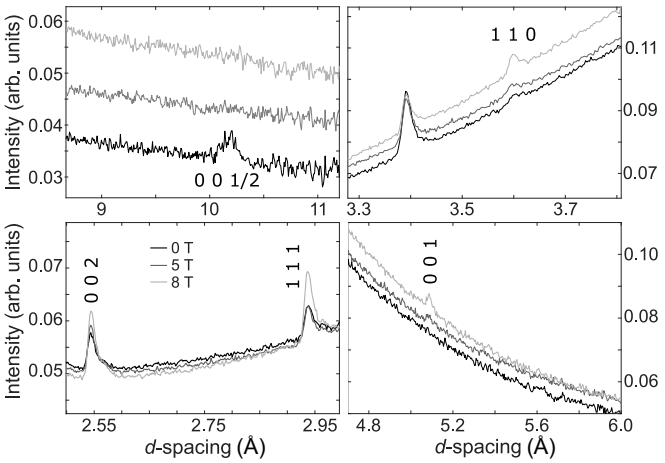

FIG. 10. Peak intensity changes as a function of applied field at $T = 1.5$ K. Reflection labels are in the notation of the parent unit cell.

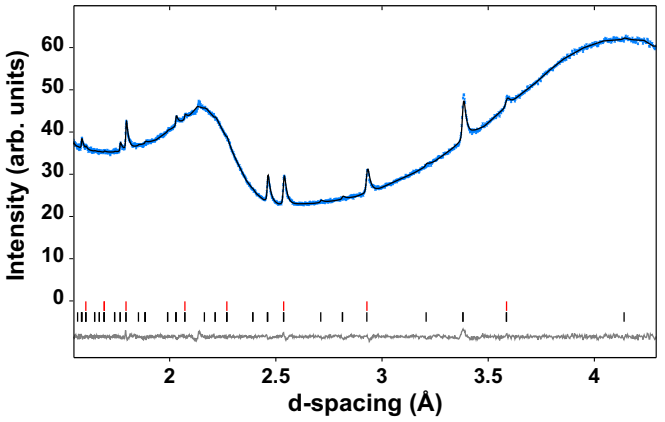

FIG. 11. A portion of the Rietveld refinement for the 1.5K 5T structure in $P4/mm'm'$ (90° bank 3 WISH). The unindexed peak at 2.14 Å is from vanadium, the substantial background is from the quartz ampoule used to contain the sample with the data in blue, calculated pattern in black, difference in gray, nuclear reflections indicated by red tickmarks and magnetic in black.

Fig. 11). At the second transition, a further arm of the star, $(0,\frac{1}{2},0)$ is lost, resulting in $Pm'm'm$ with 5 sites. With these sites again constrained to have equal moments an excellent fit is obtained, the results of which are summarized in Table V and Fig. 12. The ordered moment obtained is slightly smaller than the full ordered moment for Eu^{2+} but considering the magnetic anisotropy present, it is possible that there is a certain amount of phase coexistence in this higher-field region, which the current powder measurements are relatively insensitive to. Therefore the overall phase transition sequence can be suggested to be $P_1a\bar{3} \rightarrow P4/mm'm' \rightarrow Pm'm'm$ assuming an applied field along the (0,0,1) direction. This is justified by the impossibility of determining moment direction in a metrically cubic material from powder data. The magnetic structures of the Ferri-II and Ferri-III phases, decomposed into ferromagnetic and antiferromagnetic components, are shown in Fig. 2.

Overall, we find this sequence based on the multi-k model to be the most phenomenologically reasonable and consistent with the known interactions within the system. It is also consistent with all physical property data, including the magnitudes of the jumps in magnetization at each magnetic transition. It should be noted that single crystal measurements will be required to fully confirm the magnetic space groups and exact moment directions in all magnetic phases, but in the meantime a reasonable solution has been obtained.

TABLE IV. The results of the Rietveld refinement of the 1.5K 5T Eu_3PbO data in magnetic space group $P4/mm'm'$, a $= 2a_p$, b $= 2a_p$, and c $= a_p$, where a_p is the parent lattice constant.

Site	x	y	z	m_x (μ_B/Eu^{2+})	m_y (μ_B/Eu^{2+})	m_z (μ_B/Eu^{2+})
Eu1	0	0.5	0	0	0	6.45 ± 0.06
Eu2	0.25	0	0.5	0	0	−6.45 ± 0.06
Eu3	0.75	0.5	0.5	0	0	6.45 ± 0.06
Eu4	0.5	0.5	0.0	0	0	6.45 ± 0.06
Eu5	0	0	0	0	0	−6.45 ± 0.06

APPENDIX D: TIGHT-BINDING MODEL FOR Eu_3PbO

To construct a tight-binding model for Eu_3PbO we follow along the lines of the works by Kariyado and Ogata [56] and Chiu *et al.* [57]. In Ref. [57], a nine-band model for Ca_3PbO with three Pb-p orbitals and six Ca-d orbitals was constructed. This model captures the low-energy physics of Ca_3PbO faithfully. In particular, it exhibits six gapped Dirac cones along the Γ-X direction with a nonzero mirror Chern number, in full agreement with the *ab initio* DFT calculations. In the following, we describe how this model can be adapted to the case of Eu_3PbO, both for the paramagnetic phase and the magnetically ordered phases.

1. Paramagnetic phase

The paramagnetic phase of Eu_3PbO can be described by the same model as in Ref. [57], albeit with different parameter values, since its band structure is qualitatively similar to Ca_3PbO. In the absence of spin-orbit coupling, this tight-binding model is written as $\mathcal{H}_{\rm PM} = \sum_{\mathbf{k}} \psi^\dagger_{\mathbf{k}} H_{\rm PM}(\mathbf{k}) \psi_{\mathbf{k}}$ with the nine-component spinor

$$\psi_{\mathbf{k}} = \big(\mathrm{Pb}_{p_x},\ \mathrm{Pb}_{p_y},\ \mathrm{Pb}_{p_z},\ \mathrm{Eu}^1_{d_{y^2-z^2}},\ \times \mathrm{Eu}^2_{d_{z^2-x^2}},\ \mathrm{Eu}^3_{d_{x^2-y^2}},\ \mathrm{Eu}^1_{d_{yz}},\ \mathrm{Eu}^2_{d_{zx}},\ \mathrm{Eu}^3_{d_{xy}}\big)^{\mathrm{T}}$$

TABLE V. The results of the Rietveld refinement of the 1.5K 8T Eu_3PbO data in magnetic space group $Pm'm'm$, a $= 2a_p$, b $= a_p$, and c $= a_p$, where a_p is the parent lattice constant.

Site	x	y	z	m_x (μ_B/Eu^{2+})	m_y (μ_B/Eu^{2+})	m_z (μ_B/Eu^{2+})
Eu1	0	0.5	0.5	0	0	5.08 ± 0.06
Eu2	0.25	0	0.5	0	0	−5.08 ± 0.06
Eu3	0.25	0.5	0	0	0	−5.08 ± 0.06
Eu4	0.75	0	0.5	0	0	5.08 ± 0.06
Eu5	0.75	0.5	0	0	0	5.08 ± 0.06

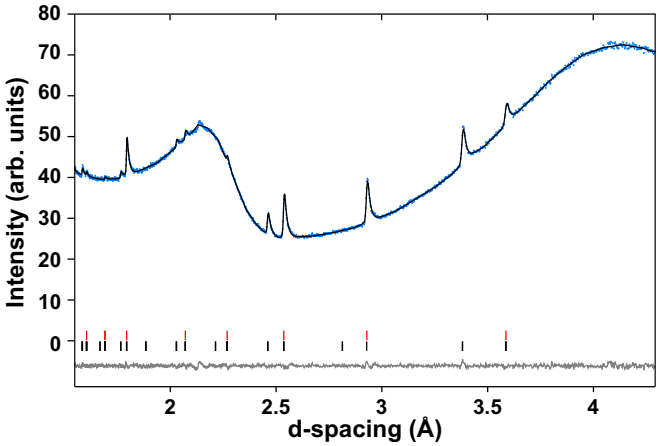

FIG. 12. A portion of the Rietveld refinement for the 1.5K 8T structure in $Pm'm'm$ (90° bank 3 WISH). The unindexed peak at 2.14 Å is from vanadium, the substantial background is from the quartz ampoule used to contain the sample with the data in blue, calculated pattern in black, difference in gray, nuclear reflections indicated by red tickmarks and magnetic in black.

and the 9×9 matrix $H_{\mathrm{PM}}(\mathbf{k})$ with block form

$$H_{\mathrm{PM}}(\mathbf{k}) = \begin{pmatrix} H_p & V_{dp}^{u} & V_{dp}^{l} \\ V_{dp}^{u\,\dagger} & H_d^u & 0 \\ V_{dp}^{l\,\dagger} & 0 & H_d^l \end{pmatrix}. \tag{D1}$$

The blocks of $H_{\mathrm{PM}}(\mathbf{k})$ are given by

$$H_p = \begin{pmatrix} e_p - 2t_{pp}c_{2x} & 0 & 0 \\ 0 & e_p - 2t_{pp}c_{2y} & 0 \\ 0 & 0 & e_p - 2t_{pp}c_{2z} \end{pmatrix}, \tag{D2}$$

$$H_d^u = \begin{pmatrix} e_d & -4t_{dd}c_xc_y & -4t_{dd}c_zc_x \\ -4t_{dd}c_xc_y & e_d & -4t_{dd}c_yc_z \\ -4t_{dd}c_zc_x & -4t_{dd}c_yc_z & e_d \end{pmatrix}, \tag{D3}$$

and $H_d^l = e_d \mathbb{1}_3$, with $\mathbb{1}_3$ the 3×3 identity matrix. The coupling matrices between Pb-p and Eu-d orbitals read

$$V_{dp}^{u} = 4it_{pd}\begin{pmatrix} 0 & c_zs_x & -c_ys_x \\ -c_zs_y & 0 & c_xs_y \\ c_ys_z & -c_xs_z & 0 \end{pmatrix},$$

$$V_{dp}^{l} = 4it_{pd}\begin{pmatrix} 0 & c_xs_z & c_xs_y \\ c_ys_z & 0 & c_ys_x \\ c_zs_y & c_zs_x & 0 \end{pmatrix}, \tag{D4}$$

where we have used the abbreviations $c_i = \cos\frac{k_i}{2}$, $s_i = \sin\frac{k_i}{2}$, and $c_{2i} = \cos k_i$.

To lowest order, spin-orbit coupling enters as an on-site term in the tight-binding Hamiltonian (D1). For the Pb-p orbitals, the on-site spin-orbit coupling reads $\sum_{\mathbf{k}} \psi_p^\dagger(\mathbf{k}) H_{\mathrm{SO}}^p(\mathbf{k}) \psi_p(\mathbf{k})$ with the spinor

$$\psi_p(\mathbf{k}) = (\mathrm{Pb}_{p_x}^{\uparrow}, \mathrm{Pb}_{p_y}^{\uparrow}, \mathrm{Pb}_{p_z}^{\uparrow}, \mathrm{Pb}_{p_x}^{\downarrow}, \mathrm{Pb}_{p_y}^{\downarrow}, \mathrm{Pb}_{p_z}^{\downarrow})$$

and

$$H_{\mathrm{SO}}^p(\mathbf{k}) = \frac{\lambda_p}{2}\begin{pmatrix} 0 & -i & 0 & 0 & 0 & 1 \\ i & 0 & 0 & 0 & 0 & -i \\ 0 & 0 & 0 & -1 & i & 0 \\ 0 & 0 & -1 & 0 & i & 0 \\ 0 & 0 & -i & -i & 0 & 0 \\ 1 & i & 0 & 0 & 0 & 0 \end{pmatrix}.$$

The on-site spin-orbit coupling for the Eu-d orbitals is $\sum_{\mathbf{k}} \psi_d^\dagger(\mathbf{k}) H_{\mathrm{SO}}^d(\mathbf{k}) \psi_d(\mathbf{k})$ with the vector

$$\begin{aligned}\psi_d(\mathbf{k}) &= \big(\mathrm{Eu}_{d_{y^2-z^2}}^{1,\uparrow}, \mathrm{Eu}_{d_{z^2-x^2}}^{2,\uparrow}, \mathrm{Eu}_{d_{x^2-y^2}}^{3,\uparrow}, \mathrm{Eu}_{d_{y^2-z^2}}^{1,\downarrow}, \mathrm{Eu}_{d_{z^2-x^2}}^{2,\downarrow}, \\ &\quad \times \mathrm{Eu}_{d_{x^2-y^2}}^{3,\downarrow}, \mathrm{Eu}_{d_{yz}}^{1,\uparrow}, \mathrm{Eu}_{d_{zx}}^{2,\uparrow}, \mathrm{Eu}_{d_{xy}}^{3,\uparrow}, \mathrm{Eu}_{d_{yz}}^{1,\downarrow}, \mathrm{Eu}_{d_{zx}}^{2,\downarrow}, \mathrm{Eu}_{d_{xy}}^{3,\downarrow}, \big)^T,\end{aligned}$$

and

$$\begin{aligned}H_{\mathrm{SO}}^d(\mathbf{k}) =& \lambda_d \tau_y \otimes \left\{ \sigma_x \otimes \begin{pmatrix} 1 & 0 & 0 \\ 0 & 0 & 0 \\ 0 & 0 & 0 \end{pmatrix} \right. \\ &\left. + \sigma_y \otimes \begin{pmatrix} 0 & 0 & 0 \\ 0 & 1 & 0 \\ 0 & 0 & 0 \end{pmatrix} + \sigma_z \otimes \begin{pmatrix} 0 & 0 & 0 \\ 0 & 0 & 0 \\ 0 & 0 & 1 \end{pmatrix} \right\},\end{aligned} \tag{D5}$$

where τ_β and σ_α operate on the d orbital ($d_{x_i^2-x_j^2}$ and $d_{x_ix_j}$) and spin ($\uparrow$ and $\downarrow$) degree of freedom, respectively. Combining these spin-orbit coupling terms with Eq. (D1), we obtain the full tight-binding Hamiltonian for the paramagnetic phase of Eu_3PbO

$$H_{\mathrm{PM}}^{\mathrm{tot}}(\mathbf{k}) = \begin{pmatrix} H_p^{\mathrm{tot}}(\mathbf{k}) & V_{\mathrm{tot}}(\mathbf{k}) \\ V_{\mathrm{tot}}^\dagger(\mathbf{k}\hat{E}) & H_d^{\mathrm{tot}}(\mathbf{k}) \end{pmatrix} + \mu \mathbb{1}_{18}, \tag{D6}$$

with

$$\begin{aligned}H_p^{\mathrm{tot}}(\mathbf{k}) &= \begin{pmatrix} H_p & 0 \\ 0 & H_p \end{pmatrix} + H_{\mathrm{SO}}^p(\mathbf{k}), \\ H_d^{\mathrm{tot}}(\mathbf{k}) &= \begin{pmatrix} \sigma_0 \otimes H_d^u & 0 \\ 0 & \sigma_0 \otimes H_d^l \end{pmatrix} + H_{\mathrm{SO}}^d(\mathbf{k}),\end{aligned} \tag{D7}$$

and

$$V_{\mathrm{tot}}(\mathbf{k}) = \begin{pmatrix} \sigma_0 \otimes V_{dp}^u & \sigma_0 \otimes V_{dp}^l \end{pmatrix}.$$

The outermost grading of H_p^{tot} and σ_0 in Eq. (D7) corresponds to the spin grading. In Eq. (D6) a diagonal term $\mu \mathbb{1}_{18}$ for the chemical potential has been added.

We have determined the eight parameters of the above tight-binding model by a fit to the *ab initio* DFT band

structure, which yields

$$e_p = 0.0, \quad e_d = 2.4, \quad t_{pp} = -0.4, \quad t_{dd} = -0.4,$$
$$t_{pd} = -0.4, \quad \lambda_p = 0.75, \quad \lambda_d = 0.07, \quad \mu = 0.87.$$

2. Magnetic phases

To describe the Eu magnetic moments we introduce the magnetic splitting derived by the DFT calculations as Zeeman terms $H_{\mathrm{Zee},n}$ for each orbital n into the tight-binding model as

$$H_{\mathrm{Zee},n} = \left(\begin{pmatrix} \sigma_x \\ \sigma_y \\ \sigma_z \end{pmatrix} \cdot B_n \right) |n\rangle\langle n|, \tag{D8}$$

where $|n\rangle\langle n|$ is the projector onto the orbitals n without spin degree of freedom. The Pauli matrices σ_i describe the spin degree of freedom and B_n is the magnetic splitting energy.

The magnitude of the splitting energy B_n for the different orbitals is determined from the DFT calculations of the ferromagnetic phase. For the other magnetic phases we then assume that the splitting vector B_n reorients according to the respective magnetic structure, but does not change its magnitude. We have checked that this procedure leads to a tight-binding band structure that is qualitatively similar to the DFT electronic bands.

a. Ferromagnetic phase

In the ferromagnetic phase, all moments are aligned collinearly. Therefore B_n points in the same direction $\hat{B}$ at all sites and we can write $B_n = B_n\hat{B}$. By comparing to DFT calculations, we find that the magnetic splitting B_n of the different orbitals are

$$B_{\mathrm{Eu}} = 0.43\ \mathrm{eV}, \quad B_{\mathrm{Pb}} = -0.035\ \mathrm{eV}, \tag{D9}$$

which corresponds to half the total energy splitting, as read out from the DFT band structures.

In the ferromagnetic phase, the magnetization direction $\hat{B}$ can be easily aligned by the external field. As explained in the main text, the topology of the electronic bands changes with magnetization direction. In particular, the position of the Weyl points, both in energy and momentum, as well as their multiplicities depend strongly on the magnetization direction. This is shown in Table VI for the three magnetization directions [100], [110], and [111], see also Fig. 3 in the main text. Note that the Weyl points W1 only exist for the [110] and [111] magnetizations, but are absent for the [100] magnetization. For the [110] magnetization W1 has multiplicity four, i.e., there are two pairs of Weyl points, one close to the k_x axis and another one close to the k_y axis. For the [111] magnetization there are six Weyl points W1, as the symmetry is higher. That is, there is one pair of Weyl points close to each of the three mains axis k_x, k_y, and k_z. Similarly, the multiplicity of the Weyl points W2 and W3 is only four for the [110] magnetization, while it is six for the [111] magnetization. For the [110] magnetization, the Weyl points W4 have also multiplicity four, but now they are located close to the k_z axis, one pair with positive k_z and one pair with negative k_z.

TABLE VI. Weyl points of the ferromagnetic phase for different field orientations. This table lists the positions and energies of the topological band crossings in the first Brillouin zone (BZ) for the ferromagnetic phase with magnetization in [100], [110], and [111] direction (FM [100], FM [110], and FM [111], respectively). The positions of the band crossings $\mathbf{k} = (k_x, k_y, k_z)$ are given in units of $2\pi/a_i$, where a_i denotes the lattice constant of the respective real space direction. All energies are given in eV relative to the Fermi energy. The type of band crossing is indicated in the fourth column, while the fifth column states the topological invariant that protects the crossings. The last column gives the multiplicity of the crossings, i.e., the number of symmetry related crossings at the same energy.

phase	position	E (eV)	type	top. inv.	No.
FM [100]	(0.18, 0, 0)	−0.16	WP (W2)	Chern	2
FM [100]	(0.12, 0, 0)	−0.33	WP (W3)	Chern	2
FM [100]	k_yk_z plane	−0.02	Line (L1)	Berry	1
FM [100]	k_yk_z plane	−0.31	Line (L2)	Berry	1
FM [110]	(0.23, 0.015, 0)	0.06	WP (W1)	Chern	4
FM [110]	(0.19, −0.001, 0)	−0.12	WP (W2)	Chern	4
FM [110]	(0.12, 0, 0)	−0.32	WP (W3)	Chern	4
FM [110]	(0.003, 0.003, 0.13)	−0.31	WP (W4)	Chern	4
FM [110]	[110] plane	−0.02	Line (L1)	Berry	1
FM [111]	(0.23, 0.008, 0.008)	0.05	WP (W1)	Chern	6
FM [111]	(0.2, −0.001, −0.001)	−0.09	WP (W2)	Chern	6
FM [111]	(0.13, 0, 0)	−0.31	WP (W3)	Chern	6

The ferromagnetic phases with [100] and [110] magnetization exhibit also nodal lines. These nodal lines are located in the plane perpendicular to the magnetization direction, i.e., in the k_yk_z plane and in the [110] plane, respectively. These nodal lines are protected by mirror symmetry and by a quantized π-Berry phase.

b. Antiferromagnetic phase

The magnetic space group of the AFM-I phase is $P_1a\bar{3}$ (No. 205.36, type IV). The unit cell is eightfold enlarged as compared to the paramagnetic phase. That is, it is doubled in each of the three main axes x, y, and z. This leads to an eightfold back folding of the bands, and hence the tight-binding model of the AFM-I phase has $8 \times 18 = 144$ bands (including spin). Correspondingly, there are eight times more orbitals in the tight-binding model, leading to an 144×144 tight-binding Hamiltonian. The hopping parameters for this enlarged Hamiltonian can be determined in an automatized fashion directly in momentum space from the tight-binding model of the paramagnetic phase, Eq. (D6). For that purpose, we first perform a unitary transformation of Hamiltonian (D6) in order to simplify its momentum dependence. This transformation amounts to multiplying the Pb-p orbitals by $e^{i(k_x+k_y+k_z)/2}$, the Eu^1-d orbitals by $e^{ik_x/2}$, the Eu^2-d orbitals by $e^{ik_y/2}$, and the Eu^3-d orbitals by $e^{ik_z/2}$. With this, all the terms in Eq. (D6) of the form $e^{ik_n/2}$ are transformed into terms with e^{ik_n} or terms that are independent of k_n. Now, we can start to construct the tight-binding Hamiltonian for the AFM-I phase, which has a block structure with 8×8 blocks, where each

block is an 18 × 18 matrix, i.e.,

$$H_{\mathrm{AFM}}(\mathbf{k}) = \begin{pmatrix} H_{000} & H_x(\mathbf{k}) & H_y(\mathbf{k}) & H_{xy}(\mathbf{k}) & H_z(\mathbf{k}) & H_{xz}(\mathbf{k}) & H_{yz}(\mathbf{k}) & 0 \\ & H_{100} & H_y^x(\mathbf{k}) & H_y(\mathbf{k}) & H_x^z(\mathbf{k}) & H_z(\mathbf{k}) & 0 & H_{yz}(\mathbf{k}) \\ & & H_{010} & H_x(\mathbf{k}) & H_z^y(\mathbf{k}) & 0 & H_z(\mathbf{k}) & H_{xz}(\mathbf{k}) \\ & & & H_{110} & 0 & H_z^y(\mathbf{k}) & H_x^z(\mathbf{k}) & H_z(\mathbf{k}) \\ & & & & H_{001} & H_x(\mathbf{k}) & H_y(\mathbf{k}) & H_{xy}(\mathbf{k}) \\ & & \text{H.c.} & & & H_{101} & H_y^x(\mathbf{k}) & H_y(\mathbf{k}) \\ & & & & & & H_{011} & H_x(\mathbf{k}) \\ & & & & & & & H_{111} \end{pmatrix}. \tag{D10}$$

The 18 × 18 matrices H_{abc} (with $a, b, c \in \{0, 1\}$) on the diagonal describe hoppings within each of the eight paramagnetic unit cells. The off-diagonal entries H_x, H_y, H_z, H_{xy}, H_{xz}, H_{yz}, H_y^x, H_x^z, and H_z^y describe hoppings that connect different paramagnetic unit cells. These hopping terms are modified by exponential factors e^{ik_n}, since they connect different paramagnetic unit cells.

So far, Eq. (D10) represents just an artificial increase of the Hamiltonian, that trivially leads to folded bands. But now, we introduce the magnetic splitting $B_i = B_{\mathrm{Eu}}\hat{B}_i$ due to the antiferromagnetically ordered Eu moments. These splitting energies are added to the diagonal blocks H_{abc} in Eq. (D10) and have all the same magnitude

$$B_{\mathrm{Eu}} = 0.45\ \mathrm{eV}. \tag{D11}$$

The orientation of the $\hat{B}_n$ vectors on the different Eu sites is determined by the AFM ordering pattern, as given in the main text. We can implement this pattern in the following way

$$\begin{aligned} \hat{B}_{\mathrm{Eu}^1} &= \frac{1}{\sqrt{2}}(0, (-1)^a, (-1)^b), \\ \hat{B}_{\mathrm{Eu}^2} &= \frac{1}{\sqrt{2}}((-1)^c, (-1)^a, 0), \\ \hat{B}_{\mathrm{Eu}^3} &= \frac{1}{\sqrt{2}}((-1)^c, 0, (-1)^b), \end{aligned} \tag{D12}$$

where the indices $a, b, c \in \{0, 1\}$ label the eight different paramagnetic unit cells.

We note that due to backfolding, the bands in the AFM-I phase exhibit band crossings at the time-reversal invariant momenta X, Y, and Z (D2 in Fig. 3(b) of the main text). Hybridization at these points is strongly suppressed by symmetry. To explain this, we first note that the bands at the X, Y, and Z points have almost exclusively Pb-p orbital character, with only very small admixtures of Eu-d orbital character. Now, due to the combination of inversion and nonsymmorphic time-reversal symmetry $\widetilde{\mathcal{T}}$, the Pb-p orbitals cannot carry a finite magnetic moment. Hence, the splitting of the bands at the X, Y, and Z points is negligibly small, leading to nearly gapless Dirac points. From our DFT and tight-binding calculations we find that the gap of these Dirac points is indeed small, namely smaller than 1 meV. This small gap is caused by a very small, but finite, admixture of Eu-d orbital character.

APPENDIX E: TOPOLOGICAL INVARIANTS, ANOMALOUS HALL CONDUCTIVITY, AND SURFACE STATES

Here, we explain how the Chern numbers, the anomalous Hall conductivities, and the surface states are computed. We also give a detailed symmetry analysis of the anomalous Hall conductivity tensor and determine the contributions of the different Weyl points to the anomalous Hall conductivity.

1. Chern number

The numerical computation of the Chern number follows the approach of Fukui *et al.* [75]. This approach uses the U(1) link variable $U_\mu(\mathbf{k}_l)$ on a discretized Brillouin zone to define the lattice field strength $\tilde{F}_{12}(\mathbf{k}_l)$, which represents a small Wilson loop for one eigenstate of the Hamiltonian. The Chern number is then the sum over all occupied bands and all points in the two-dimensional Brillouin zone. The link variable and the lattice field strength are defined as

$$U_\mu(\mathbf{k}_l) = \frac{\langle n(\mathbf{k}_l)|n(\mathbf{k}_l + \hat{\mu})\rangle}{|\langle n(\mathbf{k}_l)|n(\mathbf{k}_l + \hat{\mu})\rangle|} \tag{E1}$$

and

$$\tilde{F}_{12}(\mathbf{k}_l) = \ln\left(U_1(\mathbf{k}_l)U_2(\mathbf{k}_l + \hat{1})U_1(\mathbf{k}_l + \hat{2})^{-1}U_2(\mathbf{k}_l)^{-1}\right),$$

respectively, where $|n(k_l)\rangle$ is the eigenstate for the nth nondegenerate band at point $\mathbf{k}_l$ in the Brillouin zone. $\hat{\mu}$ as well as the explicit versions $\hat{1}$ and $\hat{2}$ denote steps in the discretized Brillouin zone, which form a basis of the lattice. With this, the Chern number of the nth band is given by

$$C_n = \frac{1}{2\pi i}\sum_l \tilde{F}_{12}(\mathbf{k}_l), \tag{E2}$$

where the sum is over all $\mathbf{k}_l$ points in a two-dimensional Brillouin zone.

To compute the chiralities of the Weyl points in the ferri- and ferromagnetic phases, we choose a small two-dimensional sphere that encloses the given Weyl point and then perform the sum in Eq. (E2) over all $\mathbf{k}_l$ points on this two-dimensional sphere. The sign of the resulting integer is equal to the chirality of the Weyl point.

The mirror Chern number can be calculated in a similar way, namely, as the Chern number in the subspace of occupied states with equal mirror symmetry eigenvalue, see Ref. [57].

2. Anomalous Hall conductivity

Weyl points act as sources and sinks of Berry curvature. It is well known that in the presence of nonzero Berry curvature a nontrivial electronic response can be expected, i.e., an anomalous Hall conductivity. That is, the conductivity tensor σ_{ij}, defined by the relation $j_i = \sigma_{ij}E_j$ between the electrical current density j and the electric field E, contains a contribution from the anomalous Hall effect. This contribution is proportional to the momentum integral of the Berry curvature and can be written as [76]

$$\sigma_{ij} = -2\frac{e^2}{\hbar}\int \frac{\mathrm{d}^3k}{(2\pi)^3}\sum_n f(E_n(k)) \times \sum_{m\neq n}\frac{\Im\left(\langle n|\frac{\partial H(k)}{\partial k_i}|m\rangle\langle m|\frac{\partial H(k)}{\partial k_j}|n\rangle\right)}{(E_n(\mathbf{k})-E_m(\mathbf{k}))^2}, \tag{E3}$$

where $E_n(k)$ and $|n\rangle$ are the eigenenergy and eigenstate of the n-th band, respectively, and $f(E_n(k))$ is the Fermi-Dirac distribution function. For the numerical evaluation of σ_{ij} in the FM phase, the integral in Eq. (E3) is approximated by its Riemann sum, i.e., $\int \frac{\mathrm{d}^3k}{(2\pi)^3} \to \sum_{\mathbf{k}} \frac{1}{(aN)^3}$, where $a = 5.09$ Å is the lattice constant of Eu_3PbO [51] and N is the number of k points per reciprocal lattice direction.

a. Symmetries of the anomalous Hall conductivity tensor

The anomalous Hall conductivity tensor is an antisymmetric matrix of the form

$$\sigma_{\text{general}} = \begin{pmatrix} 0 & \sigma_{xy} & -\sigma_{zx} \\ -\sigma_{xy} & 0 & \sigma_{yz} \\ \sigma_{zx} & -\sigma_{yz} & 0 \end{pmatrix}, \tag{E4}$$

where the three components σ_{xy}, σ_{zx}, and σ_{yz} are, in the absence of symmetries, independent of each other. However, the magnetic space group symmetries put some constrains on this expression. To derive these constraints, we first need to consider how the symmetries act on the Berry curvature

$$\Omega^n_{ij}(\mathbf{k}) = \sum_{m\neq n}\frac{2\Im\left(\langle n|\frac{\partial H(k)}{\partial k_i}|m\rangle\langle m|\frac{\partial H(k)}{\partial k_j}|n\rangle\right)}{(E_n(\mathbf{k})-E_m(\mathbf{k}))^2}. \tag{E5}$$

First of all, we note that the Berry curvature is even under inversion, $\Omega^n_{ij}(\mathbf{k}) = \Omega^n_{ij}(-\mathbf{k})$, but odd under time-reversal symmetry $\Omega^n_{ij}(\mathbf{k}) = -\Omega^n_{ij}(-\mathbf{k})$, since complex conjugation switches the sign of the imaginary part in the numerator of Eq. (E5). Hence, in the paramagnetic phase, where both of these symmetries are present, the Berry curvature is zero. In the AFM-I phase, the time-reversal symmetry $\mathcal{T}$ is broken. However, there exists a magnetic symmetry $\widetilde{\mathcal{T}}$ that combines time-reversal with a half translation along [111]. Since, the Berry curvature is odd under this symmetry $\widetilde{\mathcal{T}}$, the Berry curvature is also vanishing in the AFM-I phase. We conclude that the anomalous Hall conductivity is vanishing both in the paramagnetic phase and antiferromagnetic phase.

In contrast, the ferri- and ferromagnetic phases exhibit nonzero anomalous Hall conductivities, as in these phases both $\mathcal{T}$ and $\widetilde{\mathcal{T}}$ are broken. We will now focus on the ferromagnetic phase and study how its symmorphic unitary symmetries constrain the form of the anomalous Hall conductivity tensor (E4). A general unitary symmetry S acts on the tight-binding Hamiltonian $H(\mathbf{k})$ of the FM phase as

$$SH(\mathbf{k})S^\dagger = H(D_S\mathbf{k}), \tag{E6}$$

where D_S is the momentum space representation of S. From Eq. (E6), it follows that for every Bloch eigenstate $|n(\mathbf{k})\rangle$ with energy $E_n(\mathbf{k})$ there is a symmetry related eigenstate $|n'(D_S\mathbf{k})\rangle = S|n(\mathbf{k})\rangle$ with the same energy, i.e., $E_n(\mathbf{k}) = E_{n'}(D_S\mathbf{k})$. Therefore the band structure is symmetric with respect to the unitary symmetries S, and hence the denominator of the Berry curvature (E5) is unchanged under the action of S. The derivative terms in the numerator of Eq. (E5), on the other hand, are transformed under S as $S\frac{\partial H(k)}{\partial k_i}S^\dagger = \frac{\partial H(D_Sk)}{\partial (D_Sk_i)}$, where $\partial/\partial k_i$ and likewise $\partial/\partial(D_Sk_i)$ are directional derivatives. With this, we find that

$$\begin{aligned}\langle n(\mathbf{k})|\frac{\partial H(\mathbf{k})}{\partial k_\alpha}|m(\mathbf{k})\rangle &= \langle n(\mathbf{k})|S^\dagger S\frac{\partial H(k)}{\partial k_\alpha}S^\dagger S|m(\mathbf{k})\rangle \\ &= \langle n'(D_S\mathbf{k})|\frac{\partial H(D_Sk)}{\partial (D_Sk_\alpha)}|m'(D_S\mathbf{k})\rangle \\ &= \langle n(D_S\mathbf{k})|\frac{\partial H(D_Sk)}{\partial (D_Sk_\alpha)}|m(D_S\mathbf{k})\rangle,\end{aligned} \tag{E7}$$

where in the last line we have assumed, without loss of generality, that the Bloch eigenstates $|n(\mathbf{k})\rangle$ are sorted with increasing eigenenergies. Combining Eq. (E7) with Eq. (E3), we see that the summands in Eq. (E3) can be grouped into symmetry related pairs, namely $\Omega^n_{ij}(\mathbf{k})$ and $\Omega^n_{ij}(D_S\mathbf{k})$, whose contributions differ only by directional derivatives $\partial/\partial k_{i/j}$ and $\partial/\partial(D_Sk_{i/j})$. If S is a mirror symmetry with mirror plane perpendicular to the main axes (or a twofold rotation symmetry about a main axis), we find that $D_Sk_{i/j} = \pm k_{i/j}$, where the sign depends on whether $k_{i/j}$ is perpendicular or parallel to the mirror plane. Since there are two derivative terms in Eq. (E5), we have $\Omega^n_{ij}(\mathbf{k}) = -\Omega^n_{ij}(D_S\mathbf{k})$, when, for example, $D_Sk_i = +k_i$ but $D_Sk_j = -k_j$, and hence the corresponding component of the anomalous Hall conductivity tensor is vanishing. Similar arguments can also be constructed for the threefold and fourfold rotation symmetries of the FM phase.

Applying the above symmetry analysis to the FM phase with magnetization orientations [100], [110], and [111], we find that conductivity tensors are of the form

$$\sigma_{\text{FM100}} = \begin{pmatrix} 0 & 0 & 0 \\ 0 & 0 & \Sigma \\ 0 & -\Sigma & 0 \end{pmatrix}, \tag{E8}$$

$$\sigma_{\text{FM110}} = \begin{pmatrix} 0 & 0 & -\Sigma' \\ 0 & 0 & \Sigma' \\ \Sigma' & -\Sigma' & 0 \end{pmatrix}, \tag{E9}$$

$$\sigma_{\text{FM111}} = \begin{pmatrix} 0 & \Sigma'' & -\Sigma'' \\ -\Sigma'' & 0 & \Sigma'' \\ \Sigma'' & -\Sigma'' & 0 \end{pmatrix}, \tag{E10}$$

for some nonzero $\Sigma, \Sigma', \Sigma'' \in \mathbb{R}$. We observe that for these high-symmetry magnetization directions, the three

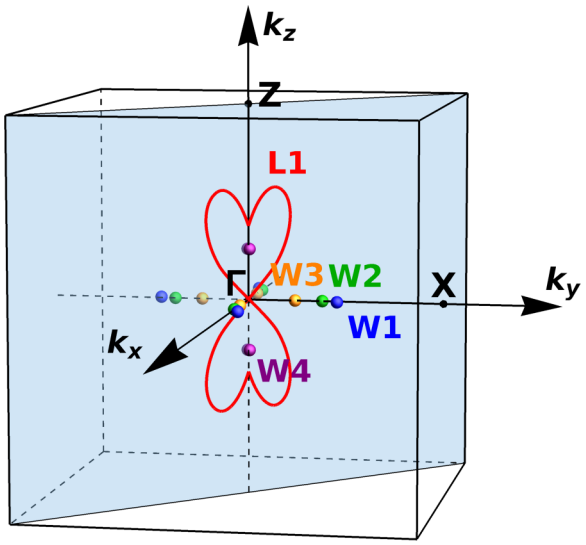

FIG. 13. Brillouin zone with nodal points (W1–W4) and the nodal line (L1) of the ferromagnetic phase for magnetic moments pointing along the [110] direction. The light blue plane corresponds to the mirror plane normal to direction of magnetic moments, in which the nodal line L1 is situated.

components of the conductivity tensor (E4) are dependent on each other.

b. Contributions of the different Weyl points to the anomalous Hall conductivity

It is known from field theoretical considerations as well as calculations in lattice systems that the conductivity of a Weyl semimetal at half-filling is given by [77]

$$\sigma_{\alpha\beta} = -\frac{e^2}{\hbar}\epsilon_{\alpha\beta\gamma}\frac{b_\gamma}{2\pi^2}, \tag{E11}$$

where $2b_\gamma$ is a component of the vector that connects the negative chirality Weyl point to the one with positive chirality. See Fig. 13 for an overview of the nodal crossings in the phase FM [110]. Note that the heart-shaped nodal line L1 does not contribute to the anomalous Hall conductivity as long as the mirror symmetry is preserved. While Eq. (E11) allows us to estimate the largest possible contribution of a pair of Weyl points to the conductivity, it gives no further information about how the conductivity depends on the chemical potential, as shown by the curves in Fig. 5 of the main text. The shape and width of the extrema of these curves depend on the details of the band structure, in particular, on how strongly the bands disperse.

Nevertheless, the location of the extrema in Fig. 5 can be explained to a large extent by the presence of Weyl points. In Table VII we list the contributions to the conductivity from the Weyl points W1, W2, and W3, as given by Eq. (E11). By comparison to Fig. 5, we can conclude that the different Weyl point contributions overlap and partially cancel. We observe that the conductivity peak of W2 spreads over a larger energy range than W1 and W3. We also note that the large positive contribution of W1 distinguishes the conductivity of FM [110] and FM [111] from FM [100].

TABLE VII. Anomalous Hall conductivity of Weyl points. This table lists the positions and energies of a selection of Weyl points in the first Brillouin zone (BZ) for the ferromagnetic phase with magnetization in [100], [110], and [111] direction (FM [100], FM [110], and FM [111], respectively). The positions of the band crossings $\mathbf{k} = (k_x, k_y, k_z)$ are given in units of $2\pi/a_i$, where a_i denotes the lattice constant of the respective real space direction. All energies are given in eV relative to the Fermi energy. The names of band crossings are indicated in the fourth column, while the fifth column states the chirality for the Weyl point at the given position. The last column gives the respective contribution to the anomalous Hall conductivity in units of $(\Omega\,\mathrm{cm})^{-1}$.

phase	position	E (eV)	name	chirality	σ_{yz}
FM [100]	(0.18, 0, 0)	−0.16	W2	1	−274
FM [100]	(0.12, 0, 0)	−0.33	W3	−1	183
FM [110]	(0.23, 0.015, 0)	0.06	W1	−1	352
FM [110]	(0.19, −0.001, 0)	−0.12	W2	1	−289
FM [110]	(0.12, 0, 0)	−0.32	W3	−1	183
FM [111]	(0.23, 0.008, 0.008)	0.05	W1	−1	351
FM [111]	(0.2, −0.001, −0.001)	−0.09	W2	1	−303
FM [111]	(0.13, 0, 0)	−0.31	W3	−1	198

3. Surface states and spin texture

To compute the surface state spectra, we perform a Fourier transform of the Hamiltonian $H(\mathbf{k})$ in the direction perpendicular to the surface, say, the z direction. This yields a Hamiltonian $H(k_x, k_y, z)$ that depends on two momenta, k_x and k_y, and on one real space coordinate z. We then numerically diagonalize the Hamiltonian $H(k_x, k_y, z)$ with open boundary conditions along the z direction, to obtain the eigenstates $\psi_n(k_x, k_y)$ and energies $E_n(k_x, k_y)$. From these we can compute the surface density of states, which is given by

$$\rho(\omega, k_x, k_y, z) = -\frac{1}{N}\mathrm{Im}\sum_n \frac{\psi_n^\dagger(k_x, k_y, z)\psi_n(k_x, k_y, z)}{\omega + i\Gamma/N - E_n(k_x, k_y)},$$
$$\rho(\omega, k_x, k_y) = \sum_{z\in\mathrm{surface}} \rho(\omega, k_x, k_y, z), \tag{E12}$$

where N denotes the number of layers perpendicular to the z direction. Here, Γ is a phenomenological broadening factor that takes into account the effects of finite temperature and disorder. For our numerical calculations we have chosen $\Gamma = 1$ and $N = 70$. The sum in the second line of Eq. (E12) is taken over the first five surface layers.

The spin polarization of the surface states is calculated very similarly by considering the weighted expectation value

$$\rho(\omega, k_x, k_y)_\alpha = -\frac{1}{N}\mathrm{Im}\sum_{n,z} \frac{\psi_n^\dagger(k_x, k_y, z)\tilde{\sigma}_\alpha\psi_n(k_x, k_y, z)}{\omega + i\Gamma/N - E_n(k_x, k_y)}, \tag{E13}$$

where $\tilde{\sigma}_\alpha$ is the spin matrix of the 18 band basis for the α direction, e.g., for $\alpha = x$, a tensor product between unity operators in orbital space and the Pauli matrix σ_x.

[1] M. Z. Hasan and C. L. Kane, Rev. Mod. Phys. **82**, 3045 (2010).

[2] X.-L. Qi and S.-C. Zhang, Rev. Mod. Phys. **83**, 1057 (2011).

[3] C.-K. Chiu, J. C. Y. Teo, A. P. Schnyder, and S. Ryu, Rev. Mod. Phys. **88**, 035005 (2016).

[4] G. E. Volovik, *Topology of Quantum Vacuum*, Lecture Notes in Physics Vol. 870 (Springer, Berlin, 2013) pp. 343–383

[5] N. P. Armitage, E. J. Mele, and A. Vishwanath, Rev. Mod. Phys. **90**, 015001 (2018).

[6] A. Burkov, Annu. Rev. Condens. Matter Phys. **9**, 359 (2018).

[7] S.-Y. Yang, H. Yang, E. Derunova, S. S. P. Parkin, B. Yan, and M. N. Ali, Adv. Phys.: X **3**, 1414631 (2018).

[8] T. Liang, Q. Gibson, M. N. Ali, M. Liu, R. J. Cava, and N. P. Ong, Nat. Mater. **14**, 280 (2015).

[9] C. Shekhar, A. K. Nayak, Y. Sun, M. Schmidt, M. Nicklas, I. Leermakers, U. Zeitler, Y. Skourski, J. Wosnitza, Z. Liu, Y. Chen, W. Schnelle, H. Borrmann, Y. Grin, C. Felser, and B. Yan, Nat. Phys. **11**, 645 (2015).

[10] S.-Y. Xu, I. Belopolski, N. Alidoust, M. Neupane, G. Bian, C. Zhang, R. Sankar, G. Chang, Z. Yuan, C.-C. Lee, S.-M. Huang, H. Zheng, J. Ma, D. S. Sanchez, B. Wang, A. Bansil, F. Chou, P. P. Shibayev, H. Lin, S. Jia, and M. Z. Hasan, Science **349**, 613 (2015).

[11] G. Bian, T.-R. Chang, H. Zheng, S. Velury, S.-Y. Xu, T. Neupert, C.-K. Chiu, S.-M. Huang, D. S. Sanchez, I. Belopolski, N. Alidoust, P.-J. Chen, G. Chang, A. Bansil, H.-T. Jeng, H. Lin, and M. Z. Hasan, Phys. Rev. B **93**, 121113(R) (2016).

[12] M. N. Ali, L. M. Schoop, C. Garg, J. M. Lippmann, E. Lara, B. Lotsch, and S. S. Parkin, Sci. Adv. **2**, e1601742 (2016).

[13] X. Wang, X. Pan, M. Gao, J. Yu, J. Jiang, J. Zhang, H. Zuo, M. Zhang, Z. Wei, W. Niu *et al.*, Adv. Electron. Mater. **2**, 1600228 (2016).

[14] R. Singha, A. K. Pariari, B. Satpati, and P. Mandal, Proc. Natl. Acad. Sci. USA **114**, 2468 (2017).

[15] X. Huang, L. Zhao, Y. Long, P. Wang, D. Chen, Z. Yang, H. Liang, M. Xue, H. Weng, Z. Fang, X. Dai, and G. Chen, Phys. Rev. X **5**, 031023 (2015).

[16] C.-L. Zhang, S.-Y. Xu, I. Belopolski, Z. Yuan, Z. Lin, B. Tong, G. Bian, N. Alidoust, C.-C. Lee, S.-M. Huang, T.-R. Chang, G. Chang, C.-H. Hsu, H.-T. Jeng, M. Neupane, D. S. Sanchez, H. Zheng, J. Wang, H. Lin, C. Zhang, H.-Z. Lu, S.-Q. Shen, T. Neupert, M. Zahid Hasan, and S. Jia, Nat. Commun. **7**, 10735 (2016).

[17] W. B. Rui, Y. X. Zhao, and A. P. Schnyder, Phys. Rev. B **97**, 161113(R) (2018).

[18] A. H. Castro Neto, F. Guinea, N. M. R. Peres, K. S. Novoselov, and A. K. Geim, Rev. Mod. Phys. **81**, 109 (2009).

[19] X. Wan, A. M. Turner, A. Vishwanath, and S. Y. Savrasov, Phys. Rev. B **83**, 205101 (2011).

[20] A. A. Burkov, M. D. Hook, and L. Balents, Phys. Rev. B **84**, 235126 (2011).

[21] S. M. Young, S. Zaheer, J. C. Y. Teo, C. L. Kane, E. J. Mele, and A. M. Rappe, Phys. Rev. Lett. **108**, 140405 (2012).

[22] L. S. Xie, L. M. Schoop, E. M. Seibel, Q. D. Gibson, W. Xie, and R. J. Cava, APL Mater. **3**, 083602 (2015).

[23] Y.-H. Chan, C.-K. Chiu, M. Y. Chou, and A. P. Schnyder, Phys. Rev. B **93**, 205132 (2016).

[24] A. Yamakage, Y. Yamakawa, Y. Tanaka, and Y. Okamoto, J. Phys. Soc. Jpn. **85**, 013708 (2016).

[25] T. T. Heikkilä and G. E. Volovik, JETP Lett. **93**, 59 (2011).

[26] M. G. Vergniory, L. Elcoro, F. Orlandi, B. Balke, Y.-H. Chan, J. Nuss, A. P. Schnyder, and L. M. Schoop, Eur. Phys. J. B **91**, 213 (2018).

[27] B. A. Bernevig, C. Felser, and H. Beidenkopf, Nature (London) **603**, 41 (2022).

[28] S. Nie, Y. Sun, F. B. Prinz, Z. Wang, H. Weng, Z. Fang, and X. Dai, Phys. Rev. Lett. **124**, 076403 (2020).

[29] S. Nie, T. Hashimoto, and F. B. Prinz, Phys. Rev. Lett. **128**, 176401 (2022).

[30] J. Li, Y. Li, S. Du, Z. Wang, B.-L. Gu, S.-C. Zhang, K. He, W. Duan, and Y. Xu, Sci. Adv. **5**, eaaw5685 (2019).

[31] C. Shekhar, N. Kumar, V. Grinenko, S. Singh, R. Sarkar, H. Luetkens, S.-C. Wu, Y. Zhang, A. C. Komarek, E. Kampert *et al.*, Proc. Natl. Acad. Sci. USA **115**, 9140 (2018).

[32] H. Su, B. Gong, W. Shi, H. Yang, H. Wang, W. Xia, Z. Yu, P.-J. Guo, J. Wang, L. Ding, L. Xu, X. Li, X. Wang, Z. Zou, N. Yu, Z. Zhu, Y. Chen, Z. Liu, K. Liu, G. Li, and Y. Guo, APL Mater. **8**, 011109 (2020).

[33] S. H. Lee, D. Graf, L. Min, Y. Zhu, H. Yi, S. Ciocys, Y. Wang, E. S. Choi, R. Basnet, A. Fereidouni *et al.*, Phys. Rev. X **11**, 031032 (2021).

[34] L. M. Schoop, A. Topp, J. Lippmann, F. Orlandi, L. Müchler, M. G. Vergniory, Y. Sun, A. W. Rost, V. Duppel, M. Krivenkov, S. Sheoran, P. Manuel, A. Varykhalov, B. Yan, R. K. Kremer, C. R. Ast, and B. V. Lotsch, Sci. Adv. **4**, eaar2317 (2018).

[35] S. Nakatsuji, N. Kiyohara, and T. Higo, Nature (London) **527**, 212 (2015).

[36] A. K. Nayak, J. E. Fischer, Y. Sun, B. Yan, J. Karel, A. C. Komarek, C. Shekhar, N. Kumar, W. Schnelle, J. Kübler, C. Felser, and S. S. P. Parkin, Sci. Adv. **2**, e1501870 (2016).

[37] H. Yang, Y. Sun, Y. Zhang, W.-J. Shi, S. S. P. Parkin, and B. Yan, New J. Phys. **19**, 015008 (2017).

[38] K. Kuroda, T. Tomita, M. T. Suzuki, C. Bareille, A. A. Nugroho, P. Goswami, M. Ochi, M. Ikhlas, M. Nakayama, S. Akebi, R. Noguchi, R. Ishii, N. Inami, K. Ono, H. Kumigashira, A. Varykhalov, T. Muro, T. Koretsune, R. Arita, S. Shin, T. Kondo, and S. Nakatsuji, Nat. Mater. **16**, 1090 (2017).

[39] Z. Wang, M. G. Vergniory, S. Kushwaha, M. Hirschberger, E. V. Chulkov, A. Ernst, N. P. Ong, R. J. Cava, and B. A. Bernevig, Phys. Rev. Lett. **117**, 236401 (2016).

[40] P. Puphal, V. Pomjakushin, N. Kanazawa, V. Ukleev, D. J. Gawryluk, J. Ma, M. Naamneh, N. C. Plumb, L. Keller, R. Cubitt, E. Pomjakushina, and J. S. White, Phys. Rev. Lett. **124**, 017202 (2020).

[41] J. Gaudet, H.-Y. Yang, S. Baidya, B. Lu, G. Xu, Y. Zhao, J. A. Rodriguez-Rivera, C. M. Hoffmann, D. E. Graf, D. H. Torchinsky *et al.*, Nat. Mater. **20**, 1650 (2021).

[42] X. Liu, S. Fang, Y. Fu, W. Ge, M. Kareev, J.-W. Kim, Y. Choi, E. Karapetrova, Q. Zhang, L. Gu, E.-S. Choi, F. Wen, J. H. Wilson, G. Fabbris, P. J. Ryan, J. W. Freeland, D. Haskel, W. Wu, J. H. Pixley, and J. Chakhalian, Phys. Rev. Lett. **127**, 277204 (2021).

[43] N. B. Schröter, I. Robredo, S. Klemenz, R. J. Kirby, J. A. Krieger, D. Pei, T. Yu, S. Stolz, T. Schmitt, P. Dudin *et al.*, Sci. Adv. **6**, eabd5000 (2020).

[44] D. Liu, A. Liang, E. Liu, Q. Xu, Y. Li, C. Chen, D. Pei, W. Shi, S. Mo, P. Dudin *et al.*, Science **365**, 1282 (2019).
[45] S. Borisenko, D. Evtushinsky, Q. Gibson, A. Yaresko, K. Koepernik, T. Kim, M. Ali, J. van den Brink, M. Hoesch, A. Fedorov *et al.*, Nat. Commun. **10**, 3424 (2019).
[46] P. Tang, Q. Zhou, G. Xu, and S.-C. Zhang, Nat. Phys. **12**, 1100 (2016).
[47] J. Park, G. Lee, F. Wolff-Fabris, Y. Y. Koh, M. J. Eom, Y. K. Kim, M. A. Farhan, Y. J. Jo, C. Kim, J. H. Shim, and J. S. Kim, Phys. Rev. Lett. **107**, 126402 (2011).
[48] J. Liu, J. Hu, Q. Zhang, D. Graf, H. B. Cao, S. Radmanesh, D. Adams, Y. Zhu, G. Cheng, X. Liu *et al.*, Nat. Mater. **16**, 905 (2017).
[49] L. Šmejkal, J. Železný, J. Sinova, and T. Jungwirth, Phys. Rev. Lett. **118**, 106402 (2017).
[50] J.-Z. Ma, S. M. Nie, C. J. Yi, J. Jandke, T. Shang, M. Y. Yao, M. Naamneh, L. Q. Yan, Y. Sun, A. Chikina, V. N. Strocov, M. Medarde, M. Song, Y.-M. Xiong, G. Xu, W. Wulfhekel, J. Mesot, M. Reticcioli, C. Franchini, C. Mudry, M. Müller, Y. G. Shi, T. Qian, H. Ding, and M. Shi, Sci. Adv. **5**, eaaw4718 (2019).
[51] J. Nuss, C. Mühle, K. Hayama, V. Abdolazimi, and H. Takagi, Acta Crystallographica Section B **71**, 300 (2015).
[52] A. Pertsova, R. M. Geilhufe, M. Bremholm, and A. V. Balatsky, Phys. Rev. B **99**, 205126 (2019).
[53] S. Suetsugu, K. Hayama, A. W. Rost, J. Nuss, C. Mühle, J. Kim, K. Kitagawa, and H. Takagi, Phys. Rev. B **98**, 115203 (2018).
[54] A. W. Rost, J. Kim, S. Suetsugu, V. Abdolazimi, K. Hayama, J. A. N. Bruin, C. Mühle, K. Kitagawa, A. Yaresko, J. Nuss, and H. Takagi, APL Mater. **7**, 121114 (2019).
[55] T. Kariyado and M. Ogata, J. Phys. Soc. Jpn. **80**, 083704 (2011).
[56] T. Kariyado and M. Ogata, J. Phys. Soc. Jpn. **81**, 064701 (2012).
[57] C.-K. Chiu, Y.-H. Chan, X. Li, Y. Nohara, and A. P. Schnyder, Phys. Rev. B **95**, 035151 (2017).
[58] Y. Obata, R. Yukawa, K. Horiba, H. Kumigashira, Y. Toda, S. Matsuishi, and H. Hosono, Phys. Rev. B **96**, 155109 (2017).
[59] T. H. Hsieh, J. Liu, and L. Fu, Phys. Rev. B **90**, 081112(R) (2014).
[60] J.-W. Rhim, J. Behrends, and J. H. Bardarson, Phys. Rev. B **95**, 035421 (2017).
[61] F. Lambert, A. P. Schnyder, R. Moessner, and I. Eremin, Phys. Rev. B **94**, 165146 (2016).
[62] M. Ikhlas, T. Tomita, T. Koretsune, M.-T. Suzuki, D. Nishio-Hamane, R. Arita, Y. Otani, and S. Nakatsuji, Nat. Phys. **13**, 1085 (2017).
[63] F. de Juan, A. G. Grushin, T. Morimoto, and J. E. Moore, Nat. Commun. **8**, 15995 (2017).
[64] N. Manyala, Y. Sidis, J. F. DiTusa, G. Aeppli, D. P. Young, and Z. Fisk, Nat. Mater. **3**, 255 (2004).
[65] S. Onoda, N. Sugimoto, and N. Nagaosa, Phys. Rev. Lett. **97**, 126602 (2006).
[66] K. Kim, J. Seo, E. Lee, K.-T. Ko, B. S. Kim, B. G. Jang, J. M. Ok, J. Lee, Y. J. Jo, W. Kang, J. H. Shim, C. Kim, H. W. Yeom, B. Il Min, B.-J. Yang, and J. S. Kim, Nat. Mater. **17**, 794 (2018).
[67] D. Samal, H. Nakamura, and H. Takagi, APL Mater. **4**, 076101 (2016).
[68] G. Sharma, P. Goswami, and S. Tewari, Phys. Rev. B **93**, 035116 (2016).
[69] O. K. Andersen, Phys. Rev. B **12**, 3060 (1975).
[70] V. Antonov, B. Harmon, and A. Yaresko, *Electronic Structure and Magneto-Optical Properties of Solids* (Kluwer Academic, Dordrecht, Boston, London, 2004).
[71] J. Perez-Mato, S. Gallego, E. Tasci, L. Elcoro, G. de la Flor, and M. Aroyo, Annu. Rev. Mater. Res. **45**, 217 (2015).
[72] J. M. Perez-Mato, S. V. Gallego, L. Elcoro, E. Tasci, and M. I. Aroyo, J. Phys.: Condens. Matter **28**, 286001 (2016).
[73] J. Rodríguez-Carvajal, Phys. B: Condens. Matter **192**, 55 (1993).
[74] V. Petrícek, M. Dusek, and L. Palatinus, Z. Kristallogr. - Cryst. Mater. **229**, 345 (2014).
[75] T. Fukui, Y. Hatsugai, and H. Suzuki, J. Phys. Soc. Jpn. **74**, 1674 (2005).
[76] D. Xiao, M.-C. Chang, and Q. Niu, Rev. Mod. Phys. **82**, 1959 (2010).
[77] P. Goswami and S. Tewari, Phys. Rev. B **88**, 245107 (2013).